3428 *Inorg. Chem.* **2010**, *49*, 3428–3440
DOI: 10.1021/ic902522j

Inorganic Chemistry
Article

Photoluminescent Lanthanide-Organic Bilayer Networks with 2,3-Pyrazinedicarboxylate and Oxalate

Paula C. R. Soares-Santos,[†,‡] Luís Cunha-Silva,[†,§] Filipe A. Almeida Paz,[†] Rute A. S. Ferreira,[‡] João Rocha,[†] Luís D. Carlos,[*,‡] and Helena I. S. Nogueira[*,†]

[†]*Department of Chemistry, and* [‡]*Department of Physics, CICECO, University of Aveiro, 3810-193 Aveiro, Portugal, and* [§]*REQUIMTE & Departments of Chemistry and Biochemistry, Faculty of Sciences, University of Porto, Rua do Campo Alegre, 4169-007 Porto, Portugal*

Received December 18, 2009

The hydrothermal reaction between lanthanide nitrates and 2,3-pyrazinedicarboxylic acid led to a new series of two-dimensional (2D) lanthanide-organic frameworks: $[Ln_2(2,3\text{-pzdc})_2(ox)(H_2O)_2]_n$ [where 2,3-pzdc^{2-} = 2,3-pyrazinedicarboxylate, ox^{2-} = oxalate, and Ln(III) = Ce, Nd, Sm, Eu, Gd, Tb, or Er]. The structural details of these materials were determined by single-crystal X-ray diffraction (for Ce^{3+} and Nd^{3+}) that revealed the formation of a layered structure. Cationic monolayers of $\{_{\infty}^{2}[Ln(2,3\text{-pzdc})(H_2O)]^{+}\}$ are interconnected via the ox^{2-} ligand leading to the formation of neutral $_{\infty}^{2}[Ln_2(2,3\text{-pzdc})_2(ox)(H_2O)_2]$ bilayer networks; structural cohesion of the crystalline packing is reinforced by the presence of highly directional O−H···O hydrogen bonds between adjacent bilayers. Under the employed hydrothermal conditions 2,3-pyrazinedicarboxylic acid can be decomposed into ox^{2-} and 2-pyrazinecarboxylate (2-pzc^{-}), as unequivocally proved by the isolation of the discrete complex $[Tb_2(2\text{-pzc})_4(ox)(H_2O)_6]\cdot 10H_2O$. Single-crystal X-ray diffraction of this latter complex revealed its co-crystallization with an unprecedented $(H_2O)_{16}$ water cluster. Photoluminescence measurements were performed for the Nd^{3+}, Sm^{3+}, Eu^{3+}, and Tb^{3+} compounds which show, under UV excitation at room temperature, the Ln^{3+} characteristic intra-4f^N emission peaks. The energy level of the triplet states of 2,3-pyrazinedicarboxylic acid (18939 cm^{-1}) and oxalic acid (24570 cm^{-1}) was determined from the 12 K emission spectrum of the Gd^{3+} compound. The $^5D_0$ and $^5D_4$ lifetime values (0.333 ± 0.006 and 0.577 ± 0.017 ms) and the absolute emission quantum yields (0.13 ± 0.01 and 0.05 ± 0.01) were determined for the Eu^{3+} and Tb^{3+} compounds, respectively. For the Eu^{3+} compound the energy transfer efficiency arising from the ligands' excited states was estimated (0.93 ± 0.01).

1. Introduction

The design and synthesis of multidimensional Metal-Organic Frameworks (MOFs), also designated as coordination polymers or coordination frameworks, have captivated the scientific community because of their interesting topologies and crystal packing motifs along with potential applications as functional materials.[1] More recently, lanthanide-organic frameworks (LnOFs) attracted Crystal Engineers owing to their potential optical applications and topological architectures which can be achieved by the high coordination number of lanthanides.[2−6] In this context, the synthesis and characterization of metal coordination polymers based on pyrazinedicarboxylato ligands have advanced rather rapidly in recent years. Pyrazinedicarboxylato are multifunctional ligands which have six sites for potential coordination to a metal center that contribute to increase the dimensionality of the assembled networks.[6−11] Nevertheless, in the literature dedicated to lanthanide complexes of pyrazinedicarboxylato ligands[6−8] little attention has been given to their luminescence properties.[6,7] These organic molecules may function as light-harvesting units acting as antennae and transferring the energy to the lanthanide, thus improving the photoluminescence of the materials; the so-called antenna-effect.[12]

Following our research interest on luminescent lanthanide one-dimensional (1D) coordination polymers,[3,13,14] we are

*To whom correspondence should be addressed. E-mail: helenanogueira@ua.pt (H.I.S.N.), lcarlos@ua.pt (L.D.C.). Phone: +351 234 370 727 (H.I.S.N.), +351 234 370 946 (L.D.C.). Fax: +351 234 370 084 (H.I.S.N.), +351 234 378 197 (L.D.C.).

(1) Champness, N. R. *Making Coordination Frameworks*; Wiley-VCH Verlag GmbH & Co. KGaA: Weinheim, Germany, 2007.James, S. L. *Chem. Soc. Rev.* **2003**, *32*, 276–288. Janiak, C. *Dalton Trans.* **2003**, 2781–2804. Kitagawa, S.; Kitaura, R.; Noro, S. *Angew. Chem., Int. Ed.* **2004**, *43*, 2334–2375. Li, H.; Eddaoudi, M.; O'Keeffe, M.; Yaghi, O. M. *Nature* **1999**, *402*, 276–279. Moulton, B.; Zaworotko, M. *J. Chem. Rev.* **2001**, *101*, 1629–1658. Rosi, N. L.; Eckert, J.; Eddaoudi, M.; Vodak, D. T.; Kim, J.; O'Keeffe, M.; Yaghi, O. M. *Science* **2003**, *300*, 1127–1129. Yaghi, O. M.; O'Keeffe, M.; Ockwig, N. W.; Chae, H. K.; Eddaoudi, M.; Kim, J. *Nature* **2003**, *423*, 705–714. Chandler, B. D.; Cramb, D. T.; Shimizu, G. K. H. *J. Am. Chem. Soc.* **2006**, *128*, 10403–10412. Cheetham, A. K.; Férey, G.; Loiseau, T. *Angew. Chem., Int. Ed.* **1999**, *38*, 3268–3292. Férey, G. *Chem. Soc. Rev.* **2008**, *37*, 191–214. Férey, G.; Mellot-Draznieks, C.; Serre, C.; Millange, F. *Acc. Chem. Res.* **2005**, *38*, 217–225. Livage, C.; Forster, P. M.; Guillou, N.; Tafoya, M. M.; Cheetham, A. K.; Férey, G. *Angew. Chem., Int. Ed.* **2007**, *46*, 5877–5879. Millward, A. R.; Yaghi, O. M. *J. Am. Chem. Soc.* **2005**, *127*, 17998–17999. Wong-Foy, A. G.; Matzger, A. J.; Yaghi, O. M. *J. Am. Chem. Soc.* **2006**, *128*, 3494–3495. Paz, F. A. A.; Khimyak, Y. Z.; Bond, A. D.; Rocha, J.; Klinowski, J. *Eur. J. Inorg. Chem.* **2002**, 2823–2828. Paz, F. A. A.; Klinowski, J. *Pure Appl. Chem.* **2007**, *79*, 1097–1110. Paz, F. A. A.; Rocha, J.; Klinowski, J.; Trindade, T.; Shi, F. N.; Mafra, L. *Prog. Solid State Chem.* **2005**, *33*, 113–125.

 Published on Web 03/12/2010

currently interested on increasing the dimensionality of the coordination polymers to two- (2D) or three-dimensions (3D).[5] To this purpose we selected 2,3-pyrazinedicarboxylic acid (2,3-H_2pzdc) as ligand (Scheme 1). Noteworthy, only a handful of examples of LnOFs with 2,3-H_2pzdc have been reported to date (dimensionality in parentheses): $[Ln(2,3\text{-}pzdc)(OH)(H_2O)]_n$ [Ln(III) = Er or Yb] (2D)[6] and $[Ln_2(2,3\text{-}pzdc)_3(H_2O)]_n \cdot 2H_2O$ [Ln(III) = La, Pr, Nd or Eu] (3D),[7] $[Ln_2Zn(2,3\text{-}pzdc)_4(H_2O)_6] \cdot 2H_2O$ [Ln(III) = Gd, Nd or Sm] (3D),[15] and $[Eu(2,3\text{-}pzdc)(NO_3)(phen)(H_2O)] \cdot 2H_2O$ (2D).[16]

Here we present a series of new LnOFs with 2,3-$pzdc^{2-}$ and ox^{2-}, $[Ln_2(2,3\text{-}pzdc)_2(ox)(H_2O)_2]_n$ [Ln(III) = Ce (**1**), Nd (**2**), Sm (**3**), Eu (**4**), Gd (**5**), Tb (**6**), or Er (**7**)], obtained by the hydrothermal reaction between the lanthanide nitrates and 2,3-H_2pzdc. We found that under the employed hydrothermal conditions 2,3-H_2pzdc can be decomposed into 2-pzc^- and ox^{2-} (Scheme 2), as proved by the isolation of the discrete complex $[Tb_2(2\text{-}pzc)_4(ox)(H_2O)_6] \cdot 10H_2O$ (**8**) (obtained as a secondary material).

Scheme 1

2,3-pyrazinedicarboxylic acid (2,3-H_2pzdc) 2-pyrazinecarboxylic acid (2-Hpzc)

Scheme 2

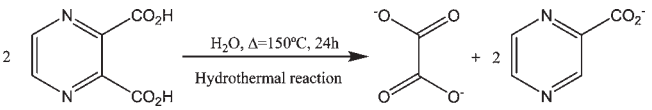

To the best of our knowledge, this is the first time that the decarboxylation of 2,3-H_2pzdc, under hydrothermal conditions, leads to the isolation of a compound (**8**) containing 2-pzc^-, unequivocally proving that 2,3-H_2pzdc is decomposed into ox^{2-} and 2-pzc^-. Lanthanide (Nd^{3+}, Eu^{3+}, Gd^{3+}, and Tb^{3+}) complexes with 2-pyrazinecarboxylic acid (2-Hpzc) have already been reported in the literature together with some photoluminescence studies.[17−19] The molecular formulas for the Eu^{3+} and Gd^{3+} complexes, $Ln(2\text{-}pzc)_3 \cdot nH_2O$, were optimized using the Sparkle model.[17] The crystal structures of $[La(2\text{-}pzc)_3(H_2O)] \cdot 2.5H_2O$[20] and $[Eu(2\text{-}pzc)_3(H_2O)_2] \cdot 6H_2O$[19] were determined, showing the three 2-pzc^{2-} ligands coordinated to the Ln^{3+} through *N,O*-chelation plus one water molecule coordinated to the La^{3+} and two water molecules coordinated to the Eu^{3+}. A mixture of 2-pzc^- and ox^{2-} was found in the 2D LnOF, $[Ln_2(2\text{-}pzc)_2(ox)_2(H_2O)_2]_n$ [Ln(III) = Pr or Er].[21]

The crystal structure of compound **8** revealed its co-crystallization with an unprecedented $(H_2O)_{16}$ water cluster. We note that interest on discrete and infinite water clusters confined in inorganic, organic, and hybrid organic−inorganic compounds has increased quite considerably in recent years, mainly because these structures may contribute to a better understanding of the behavior of water in certain biological systems.[22]

In general, all the isolated compounds **1**−**8** were structurally characterized using X-ray diffraction (XRD), elemental and thermogravimetric analyses (TGA), diffuse reflectance, scanning electron microscopy (SEM), Fourier transform infrared (FT-IR), and photoluminescence spectroscopy. Materials **1** to **7** represent the first example of bilayer networks involving 2,3-H_2pzdc in coordination polymers.

2. Experimental Section

2.1. Synthesis. $Ln(NO_3)_3 \cdot nH_2O$ and 2,3-H_2pzdc were purchased from Aldrich and were used as received. An aqueous solution (2 mL) of $Ln(NO_3)_3 \cdot nH_2O$ [Ln(III) = Ce, Nd, Sm, Eu,

(2) Allendorf, M. D.; Bauer, C. A.; Bhakta, R. K.; Houk, R. J. T. *Chem. Soc. Rev.* **2009**, *38*, 1330–1352. Guillou, O.; Daiguebonne, C. *Lanthanide-containing Coordination Polymers*; Elsevier B. V.: Amesterdam, 2005; Vol. *34*;Pan, L.; Adams, K. M.; Hernandez, H. E.; Wang, X. T.; Zheng, C.; Hattori, Y.; Kaneko, K. *J. Am. Chem. Soc.* **2003**, *125*, 3062–3067. Surble, S.; Serre, C.; Millange, F.; Pelle, F.; Férey, G. *Solid State Sci.* **2007**, *9*, 131–136. Luo, F.; Batten, S. R.; Che, Y. X.; Zheng, J. M. *Chem.—Eur. J.* **2007**, *13*, 4948–4955. Shi, F. N.; Cunha-Silva, L.; Trindade, T.; Paz, F. A. A.; Rocha, J. *Cryst. Growth Des.* **2009**, *9*, 2098–2109. Shi, F. N.; Trindade, T.; Rocha, J.; Paz, F. A. A. *Cryst. Growth Des.* **2008**, *8*, 3917–3920. Tang, S. F.; Song, J. L.; Mao, J. G. *Eur. J. Inorg. Chem.* **2006**, 2011–2019. Cunha-Silva, L.; Lima, S.; Ananias, D.; Silva, P.; Mafra, L.; Carlos, L. D.; Pillinger, M.; Valente, A. A.; Paz, F. A. A.; Rocha, J. *J. Mater. Chem.* **2009**, *19*, 2618–2632. Harbuzaru, B. V.; Corma, A.; Rey, F.; Atienzar, P.; Jorda, J. L.; Garcia, H.; Ananias, D.; Carlos, L. D.; Rocha, J. *Angew. Chem., Int. Ed.* **2008**, *47*, 1080–1083. Rodrigues, M. O.; da Costa, N. B.; de Simone, C. A.; Araujo, A. A. S.; Brito-Silva, A. M.; Paz, F. A. A.; de Mesquita, M. E.; Júnior, S. A.; Freire, R. O. *J. Phys. Chem. B* **2008**, *112*, 4204–4212. Chelebaeva, E.; Larionova, J.; Guari, Y.; Ferreira, R. A. S.; Carlos, L. D.; Paz, F. A. A.; Trifonov, A.; Guerin, C. *Inorg. Chem.* **2008**, *47*, 775–777. Chelebaeva, E.; Larionova, J.; Guari, Y.; Ferreira, R. A. S.; Carlos, L. D.; Paz, F. A. A.; Trifonov, A.; Guerin, C. *Inorg. Chem.* **2009**, *48*, 5983–5995. Harbuzaru, B. V.; Corma, A.; Rey, F.; Jorda, J. L.; Ananias, D.; Carlos, L. D.; Rocha, J. *Angew. Chem., Int. Ed.* **2009**, *48*, 6476–6479.

(3) Cunha-Silva, L.; Soares-Santos, P. C. R.; Nogueira, H. I. S.; Trindade, T.; Klinowski, J.; Filipe, J. R. A.; Paz, A. A. *Acta Crystallogr., Sect. E* **2008**, *64*, M529–M530.

(4) de Lill, D. T.; de Bettencourt-Dias, A.; Cahill, C. L. *Inorg. Chem.* **2007**, *46*, 3960–3965.

(5) Soares-Santos, P. C. R.; Cunha-Silva, L.; Paz, F. A. A.; Ferreira, R. A. S.; Rocha, J.; Trindade, T.; Carlos, L. D.; Nogueira, H. I. S. *Cryst. Growth Des.* **2008**, *8*, 2505–2516.

(6) Weng, D. F.; Zheng, X. J.; Chen, X. B.; Li, L.; Jin, L. P. *Eur. J. Inorg. Chem.* **2007**, 3410–3415.

(7) Zheng, X. J.; Jin, L. P.; Lu, S. Z. *Eur. J. Inorg. Chem.* **2002**, 3356–3363.

(8) Premkumar, T.; Govindarajan, S. *Inorg. Chem. Commun.* **2003**, *6*, 1385–1389. Zheng, X. J.; Jin, L. P. *J. Chem. Crystallogr.* **2005**, *35*, 865–869.

(9) Beobide, G.; Castillo, O.; Luque, A.; Garcia-Couceiro, U.; Garcia-Teran, J. P.; Roman, P. *Inorg. Chem.* **2006**, *45*, 5367–5382. Choi, K. Y. *J. Inclusion Phenom. Macrocyclic Chem.* **2002**, *43*, 195–199. Jaber, F.; Charbonnier, F.; Faure, R. *J. Chem. Crystallogr.* **1994**, *24*, 681–684.

(10) Wenkin, M.; Devillers, M.; Tinant, B.; Declercq, J. P. *Inorg. Chim. Acta* **1997**, *258*, 113–118.

(11) Huh, H. S.; Lee, S. W. *Bull. Korean Chem. Soc.* **2006**, *27*, 1839–1843.

(12) Lehn, J. M. *Angew. Chem., Int. Ed.* **1990**, *29*, 1304–1319.

(13) Soares-Santos, P. C. R.; Nogueira, H. I. S.; Félix, V.; Drew, M. G. B.; Ferreira, R. A. S.; Carlos, L. D.; Trindade, T. *Chem. Mater.* **2003**, *15*, 100–108.

(14) Soares-Santos, P. C. R.; Nogueira, H. I. S.; Rocha, J.; Félix, V.; Drew, M. G. B.; Ferreira, R. A. S.; Carlos, L. D.; Trindade, T. *Polyhedron* **2003**, *22*, 3529–3539. Soares-Santos, P. C. R.; Paz, F. A. A.; Ferreira, R. A. S.; Klinowski, J.; Carlos, L. D.; Trindade, T.; Nogueira, H. I. S. *Polyhedron* **2006**, *25*, 2471–2482.

(15) Cao, R.; Sun, D. F.; Liang, Y. C.; Hong, M. C.; Tatsumi, K.; Shi, Q. *Inorg. Chem.* **2002**, *41*, 2087–2094.

(16) Hu, M. L.; Yuan, J. X.; Chen, F.; Shi, Q. *Acta Crystallogr. C* **2004**, *60*, M186–M188.

(17) de Mesquita, M. E.; Silva, F.; Albuquerque, R. Q.; Freire, R. O.; da Conceição, E. C.; da Silva, J. E. C.; Júnior, N. B. C.; de Sá, G. F. *J. Alloys Compd.* **2004**, *366*, 124–131.

(18) Desa, G. F.; Neto, B. D. B.; Ferreira, R. *Inorg. Chim. Acta* **1977**, *23*, 249–252.

(19) Eliseeva, S. V.; Mirzov, O. V.; Troyanov, S. I.; Vitukhnovsky, A. G.; Kuzmina, N. P. *J. Alloys Compd.* **2004**, *374*, 293–297.

(20) Leciejewicz, J.; Ptasiewicz-Bak, H.; Premkumar, T.; Govindarajan, S. *J. Coord. Chem.* **2004**, *57*, 97–103.

(21) Li, B.; Gu, W.; Zhang, L. Z.; Qu, J.; Ma, Z. P.; Liu, X.; Liao, D. Z. *Inorg. Chem.* **2006**, *45*, 10425–10427.

(22) Infantes, L.; Chisholm, J.; Motherwell, S. *CrystEngComm* **2003**, *5*, 480–486. Ludwig, R. *Angew. Chem., Int. Ed.* **2001**, *40*, 1809–1827.

Gd, Tb, or Er; 1 mmol] was added to an aqueous solution (10 mL) of 2,3-H_2pzdc (0.252 g, 1.5 mmol). After stirring the mixture for 1 h at room temperature, it was transferred to a Parr Teflon-lined reaction vessel (ca. 25 mL, filling rate 50%) and placed inside a preheated oven at 150 °C for 24 h. The reaction vessel was cooled to room temperature, and part of the mixture was filtered and the solid obtained washed with distilled water and ethanol giving a white microcrystalline powder (**1** to **7**); the remaining part of the mixture was kept at room temperature (which, by slow evaporation, led to colorless crystals of **1** and **2**) or in the refrigerator (which led to colorless crystals of **8**). The compounds were characterized by elemental and thermogravimetric analysis, diffuse reflectance, scanning electron microscopy, FT-IR and photoluminescence spectroscopy, and XRD. The low yield obtained for compound **8** allowed the acquisition of the FT-IR and photoluminescence spectra and the single-crystal XRD only.

$[Ce_2(2,3\text{-pzdc})_2(ox)(H_2O)_2]_n$ (**1**): Anal. Calcd. (%): C, 22.83; H, 1.09; N, 7.61. Found (%): C, 22.79; H, 1.35; N, 7.32. FT-IR (KBr, cm^{-1}): 3471 (m), 1662 and 1602 (vs, $\nu_{as}CO_2^-$), 1560 (s), 1442 (s), 1432 (s), 1400 (s), 1369 and 1309 (s-m, $\nu_sCO_2^-$), 1199 (w), 1159 (w), 1112 (m), 1060 (w), 896 (m), 881 (w), 856 (m), 848 (w), 788 (m), 769 (m), 734 (m), 667 (w), 649 (w), 538 (m), 491 (w), 460 (w), 424 (vw), 412 (vw), 372 (w).

$[Nd_2(2,3\text{-pzdc})_2(ox)(H_2O)_2]_n$ (**2**): Anal. Calcd. (%): C, 22.58; H, 1.08; N, 7.52. Found (%): C, 22.60; H, 1.33; N, 7.35. FT-IR (KBr, cm^{-1}): 3484 (m), 1675, 1660, 1615, and 1604 (vs, $\nu_{as}CO_2^-$), 1560 (s), 1444 (s), 1430 (s), 1400 (s), 1371 and 1311 (s-m, $\nu_sCO_2^-$), 1201 (w), 1159 (w), 1114 (m), 1060 (w), 898 (m), 882 (w), 860 (m), 848 (w), 790 (m), 771 (m), 734 (m), 669 (w), 649 (w), 538 (m), 489 (w), 464 (w), 428 (vw), 413 (vw), 379 (w).

$[Sm_2(2,3\text{-pzdc})_2(ox)(H_2O)_2]_n$ (**3**): Anal. Calcd. (%): C, 22.21; H, 1.07; N, 7.40. Found (%): C, 22.29; H, 1.33; N, 7.25. FT-IR (KBr, cm^{-1}): 3484 (m), 1677, 1660, 1620, and 1604 (vs, $\nu_{as}CO_2^-$), 1562 (s), 1446 (s), 1430 (s), 1401 (s), 1371 and 1311 (s-m, $\nu_sCO_2^-$), 1203 (w), 1160 (w), 1114 (m), 1060 (w), 900 (m), 882 (w), 862 (m), 849 (w), 792 (m), 771 (m), 732 (m), 678 (w), 648 (w), 538 (m), 487 (w), 466 (w), 431 (vw), 415 (vw), 383 (w).

$[Eu_2(2,3\text{-pzdc})_2(ox)(H_2O)_2]_n$ (**4**): Anal. Calcd. (%): C, 21.12; H, 1.06; N, 7.37. Found (%): C, 21.44; H, 1.38; N, 7.44. FT-IR (KBr, cm^{-1}): 3484 (m), 1680, 1660, 1620, and 1606 (vs, $\nu_{as}CO_2^-$), 1562 (s), 1446 (s), 1430 (s), 1401 (s), 1371, 1362, and 1313 (s-m, $\nu_sCO_2^-$), 1203 (w), 1160 (w), 1114 (m), 1062 (w), 900 (m), 881 (w), 862 (m), 848 (w), 792 (m), 771 (m), 732 (m), 680 (w), 647 (w), 538 (m), 487 (w), 468 (w), 433 (vw), 416 (vw), 385 (w).

$[Gd_2(2,3\text{-pzdc})_2(ox)(H_2O)_2]_n$ (**5**): Anal. Calcd. (%): C, 21.82; H, 1.05; N, 7.27. Found (%): C, 22.09; H, 1.36; N, 7.21. FT-IR (KBr, cm^{-1}): 3482 (m), 1679, 1660, 1623, and 1608 (vs, $\nu_{as}CO_2^-$), 1562 (s), 1449 (s), 1430 (s), 1401 (s), 1371, 1361, and 1313 (s-m, $\nu_sCO_2^-$), 1203 (w), 1160 (w), 1114 (m), 1062 (w), 900 (m), 881 (w), 863 (m), 849 (w), 794 (m), 771 (m), 734 (m), 682 (w), 647 (w), 538 (m), 487 (w), 468 (w), 433 (vw), 417 (vw), 389 (w).

$[Tb_2(2,3\text{-pzdc})_2(ox)(H_2O)_2]_n$ (**6**): Anal. Calcd. (%): C, 21.72 ; H, 1.04; N, 7.24. Found (%): C, 21.21; H, 1.41; N, 7.37. FT-IR (KBr, cm^{-1}): 3482 (m), 1679, 1660, 1620, and 1606 (vs, $\nu_{as}CO_2^-$), 1562 (s), 1448 (s), 1430 (s), 1401 (s), 1371, 1360, and 1313 (s-m, $\nu_sCO_2^-$), 1205 (w), 1160 (w), 1114 (m), 1062 (w), 902 (m), 883 (w), 865 (m), 848 (w), 794 (m), 771 (m), 732 (m), 684 (w), 646 (w), 536 (m), 485 (w), 470 (w), 435 (vw), 418 (vw), 391 (w).

$[Er_2(2,3\text{-pzdc})_2(ox)(H_2O)_2]_n$ (**7**): Anal. Calcd. (%): C, 21.27; H, 1.02; N, 7.09. Found (%): C, 20.79; H, 1.25; N, 6.93. FT-IR (KBr, cm^{-1}): 3465 (m), 1681, 1662, 1620, and 1610 (vs, $\nu_{as}CO_2^-$), 1563 (s), 1448 (s), 1432 (s), 1403 (s), 1373, 1359, and 1315 (s-m, $\nu_sCO_2^-$), 1207 (w), 1162 (w), 1114 (m), 1062 (w), 904 (m), 882 (w), 867 (m), 846 (w), 794 (m), 769 (m), 732 (m), 682 (w), 646 (w), 536 (m), 484 (w), 474 (w), 439 (vw), 418 (vw), 399 (w).

$[Tb_2(2\text{-pzc})_4(ox)(H_2O)_6]\cdot 10H_2O$ (**8**): FT-IR (KBr, cm^{-1}): 3365 (m,b), 1619 (vs, $\nu_{as}CO_2^-$), 1581 (s), 1525 (w), 1475 (w), 1423 (m), 1374 and 1315 (s-m, $\nu_sCO_2^-$), 1290 (w), 1187 (w), 1164 (m), 1116 (vw), 1054 (w), 1035 (m), 862 (m), 794 (m), 734 (m), 543 (w), 487 (w), 451 (m), 422 (w), 393 (w).

2.2. Instrumentation. FT-IR spectra were obtained as KBr (Aldrich 99%+, FT-IR grade) pellets using a Mattson 7000 FT instrument.

Elemental analyses (C, H, and N) were performed with a CHNS-932 elemental analyzer.

TGA were carried out using a Shimadzu TGA 50, with a heating rate of 10 °C/min, under a continuous air stream with a flow rate of 10 mL/min.

SEM images were collected using Hitachi SU-70 field emission gun tungsten filament instruments working typically at 25 kV. A small drop of an ethanolic suspension of single-crystals of **1** was deposited on glass. Sprinkled powder of **4** and **6** was deposited on carbon tape. All samples were prepared on an aluminum sample holder and coated with Au/Pd.

Diffuse reflectance spectra were measured on a JASCO V-560 instrument using $BaSO_4$ as reflecting standard.

Photoluminescence spectra were recorded in the solid state, between 12 K and room temperature, with a modular double grating excitation spectrofluorimeter with a TRIAX 320 emission monochromator (Fluorolog-3, Jobin Yvon-Spex) coupled to a R928 (ultraviolet/visible) and H9170-75 (near-infrared, NIR) Hamamatsu photomultipliers. For **3**, the photoluminescence spectra were recorded at room temperature with a double grating excitation and emission spectrometer (Fluorolog-3 model FL3−22, Horiba Jobin Yvon-Spex) coupled to a R928 Hamamatsu photomultiplier. The excitation sources were a 450 W Xe arc lamp. The spectra were acquired using the front face mode and were corrected for detection and optical spectral response. Emission was corrected for the spectral response of the monochromators and the detector using typical correction spectrum provided by the manufacturer, and the excitation spectra were corrected for the spectral distribution of the lamp intensity using a photodiode reference detector. Time-resolved measurements were carried out (Fluorolog-3, Jobin Yvon-Spex) using the setup described above with a pulsed Xe−Hg lamp (6 μs pulse at half-width and 20−30 μs tail). The absolute emission quantum yields were measured at room temperature using a Quantum Yield Measurement System C9920−02 from Hamamatsu with a 150 W Xe lamp coupled to a monochromator for wavelength discrimination, an integrating sphere as sample chamber, and a multichannel analyzer for signal detection. Three measurements were made for each sample, and the average value is reported. The method is accurate to within 10%.

Powder X-ray diffraction (PXRD) data were collected at ambient temperature (ca. 298 K) on an X'Pert MPD Philips diffractometer (Cu K_α X-radiation, λ = 1.54060 Å), equipped with a X'Celerator detector, a curved graphite-monochromated radiation and a flat-plate sample holder, in a Bragg−Brentano para-focusing optics configuration (40 kV, 50 mA). Intensity data were collected in continuous scanning mode in the range of about $3 \leq 2\theta^\circ \leq 50$.

2.3. Single-Crystal X-ray Diffraction Studies. Crystalline material of $[Ln_2(2,3\text{-pzdc})_2(ox)(H_2O)_2]_n$ [where Ln(III) = Ce (**1**) or Nd (**2**)] and $[Tb_2(2\text{-pzc})_4(ox)(H_2O)_6]\cdot 10H_2O$ (**8**) suitable for single-crystal X-ray analysis were harvested and mounted on Hampton Research CryoLoops using FOMBLIN Y perfluoropolyether vacuum oil (LVAC 25/6) purchased from Aldrich with the help of a Stemi 2000 stereomicroscope equipped with Carl Zeiss lenses.[23] Complete diffraction data sets for **1** and **2** were collected at 150(2) K on a Bruker X8 Kappa APEX II charge-coupled device (CCD) area-detector diffractometer (Mo K_α graphite-monochromated radiation, λ = 0.7107 Å) controlled by the APEX2 software package,[24] and equipped with an Oxford Cryosystems Series 700 cryostream monitored remotely

(23) Kottke, T.; Stalke, D. *J. Appl. Crystallogr.* **1993**, *26*, 615–619.
(24) *APEX2 Data Collection Software*, Version 2.1-RC13; Bruker AXS: Delft, The Netherlands, 2006.

Table 1. Crystal and Structure Refinement Details for $[Ln_2(2,3\text{-pzdc})_2(ox)(H_2O)_2]_n$ [Ln(III) = Ce (**1**) or Nd (**2**)] and $[Tb_2(2\text{-pzc})_4(ox)(H_2O)_6]\cdot 10H_2O$ (**8**)

	1	**2**	**8**
formula	$C_7H_4CeN_2O_7$	$C_7H_4NdN_2O_7$	$C_{22}H_{44}N_8O_{28}Tb_2$
formula weight	368.24	372.36	1186.49
instrument	Bruker X8 APEX II	Bruker X8 APEX II	Bruker Nonius FR591
wavelength/Å	0.7107	0.7107	1.5418
crystal system	monoclinic	monoclinic	triclinic
space group	$C2/m$	$C2/m$	$P\bar{1}$
a/Å	10.8024(11)	10.6881(17)	9.7616(3)
b/Å	8.1744(11)	8.1381(15)	10.2365(3)
c/Å	11.2884(14)	11.296(3)	11.1146(3)
α/deg	90	90	77.141(2)
β/deg	105.784(6)	106.293(10)	73.644(2)
γ/deg	90	90	77.468(2)
volume/Å^3	959.2(2)	943.1(3)	1024.72(5)
Z	4	4	1
D_c/g cm^{-3}	2.550	2.623	1.923
μ(Mo−Kα)/mm^{-1}	4.775	5.535	17.693
crystal size/mm^3	0.10 × 0.02 × 0.01	0.12 × 0.10 × 0.08	0.07 × 0.05 × 0.01
crystal type	colorless plates	colorless plates	colorless plates
θ range	3.75 to 25.33	3.76 to 27.47	8.05 to 65.05
index ranges	$-12 \le h \le 12$	$-12 \le h \le 13$	$-10 \le h \le 11$
	$-9 \le k \le 9$	$-9 \le k \le 10$	$-11 \le k \le 12$
	$-13 \le l \le 13$	$-14 \le l \le 13$	$-0 \le l \le 13$
reflections collected	5353	6315	3458
independent reflections	890 (R_{int} = 0.0520)	1133 (R_{int} = 0.0725)	3458 (R_{int} = 0.0703)
data completeness	to θ = 25.33°, 94.4%	to θ = 27.47°, 97.4%	to θ = 65.05°, 98.9%
final R indices [$I > 2\sigma(I)$][a,b]	$R1$ = 0.0275	$R1$ = 0.0393	$R1$ = 0.0527
	$wR2$ = 0.0474	$wR2$ = 0.0642	$wR2$ = 0.1446
final R indices (all data)[a,b]	$R1$ = 0.0395	$R1$ = 0.0598	$R1$ = 0.0540
	$wR2$ = 0.0499	$wR2$ = 0.0690	$wR2$ = 0.1459
largest diff. peak and hole/e Å^{-3}	0.691 and −1.033	1.197 and −1.738	1.623 and −1.322

[a] $R1 = \sum||F_o| - |F_c||/\sum|F_o|$. [b] $wR2 = [\sum w(F_o^2 - F_c^2)^2/\sum w(F_o^2)^2]^{1/2}$.

by the software interface Cryopad.[25] Images were processed using the software package SAINT+,[26] and data were corrected for absorption by the multiscan semiempirical method implemented in SADABS.[27] Data for **8** were collected at room temperature (293 K) on a Bruker-Nonius FR591 Kappa CCD 2000 diffractrometer equipped with a rotating anode X-ray source (λ = 1.5418 Å), controlled by the COLLECT software package.[28] Images were processed using the software package HKL2000,[29] and data were corrected for absorption with SADABS.[27] Structures were solved using the direct methods implemented in SHELXS-97,[30] which allowed the immediate location of the majority of the heaviest atoms, with the remaining non-hydrogen atoms being directly located from difference Fourier maps calculated from successive full-matrix least-squares refinement cycles on F^2 using SHELXL-97.[31] Non-hydrogen atoms of all complexes were successfully refined using anisotropic displacement parameters.

Hydrogen atoms bonded to aromatic carbons belonging to the pyrazine ring were located at their idealized positions using the HFIX 43 instructions in SHELXL and included in subsequent refinement cycles in riding-motion approximation with isotropic thermal displacements parameters (U_{iso}) fixed at 1.2 times U_{eq} of the carbon atom to which they are attached. In **1** and **2**, the hydrogen atoms belonging to the coordinated water molecule could not be directly located from difference Fourier maps, and no attempt was made to place these in approximate calculated positions. However, they have been included in the respective molecular formulas of the compounds (Table 1). In **8**, the hydrogen atoms associated with both the coordinated [O(1W), O(2W), and O(3W)] and uncoordinated [O(4W), O(5W), O(6W), O(7W), and O(8W)] water molecules were markedly visible from difference Fourier maps, and were included in the final structural models with the O−H and H···H distances restrained to 1.00(1) and 1.63(1) Å, respectively (to ensure a chemically reasonable geometry for these molecules), assuming a riding-motion approximation with an isotropic thermal displacement parameter fixed at 1.5 times U_{eq} of the oxygen atom to which they are attached.

The last difference Fourier map synthesis showed: for **1**, the highest peak (0.691 e Å^{-3}) and deepest hole (−1.033 e Å^{-3}) located at 0.97 Å and 1.02 Å from Ce(1) and C(2), respectively; for **2**, the highest peak (1.197 e Å^{-3}) and deepest hole (−1.738 e Å^{-3}) located at 1.24 Å and 0.84 Å from Nd(1), respectively; for (**8**), the highest peak (1.623 e Å^{-3}) located at 1.20 Å and deepest hole (−1.323 e Å^{-3}) located at 0.84 Å from Tb(1).

Information concerning crystallographic data collection and structure refinement details is summarized in Table 1. Selected bond lengths and angles for the Ce^{3+} (in **1**) and Tb^{3+} (in **8**) coordination environments are collected in Tables S1 and S2 in the electronic Supporting Information, respectively. Structural drawings have been prepared using the software package Crystal Diamond.[32]

Crystallographic data (excluding structure factors) for the structures reported in this paper have been deposited with the Cambridge Crystallographic Data Centre (CCDC) as supplementary publication no. CCDC-736554 (**1**), -736555 (**2**), and -736556 (**8**). Copies of available data can be obtained free of charge on application to CCDC, 12 Union Road, Cambridge

(25) *Cryopad, Remote monitoring and control*, Version 1.451; Oxford Cryosystems: Oxford, United Kingdom, 2006.
(26) *SAINT+ Data Integration Engine*, v. 7.23a; Bruker AXS: Madison, WI, 1997−2005.
(27) Sheldrick, G. M. *SADABS v.2.01, Bruker/Siemens Area Detector Absorption Correction Program*; Bruker AXS: Madison, WI, 1998.
(28) Hooft, R. *Collect: Data Collection Software*; Nonius B. V.: Delft, The Netherlands, 1998.
(29) Otwinowski, Z.; Minor, W. In *Methods Enzymol.*; Carter, C. W., Jr., Sweet, R. M., Eds.; Academic Press: New York, 1997; Vol. *276*, p 307.
(30) Sheldrick, G. M. *SHELXS-97, Program for Crystal Structure Solution*; University of Göttingen: Göttingen, Germany, 1997.
(31) Sheldrick, G. M. *SHELXL-97, Program for Crystal Structure Refinement*, University of Göttingen: Göttingen, Germany, 1997.
(32) Brandenburg, K. *DIAMOND*, Version 3.2; Crystal Impact GbR: Bonn, Germany, 2006.

CB2 2EZ, U.K.; Fax: (+44) 1223 336033, or online via www.ccdc.cam.ac.uk/data_request/cif or by emailing data_request@ccdc.cam.ac.uk.

3. Results and Discussion

3.1. Preparation of the Materials. A series of new 2D lanthanide-organic frameworks (LnOFs) were prepared by hydrothermal reaction of the lanthanide(III) nitrates with 2,3-H_2pzdc, at 150 °C during 24 h, $[Ln_2(2,3\text{-pzdc})_2(ox)(H_2O)_2]_n$ [Ln(III) = Ce (**1**), Nd (**2**), Sm (**3**), Eu (**4**), Gd (**5**), Tb (**6**), or Er (**7**)]. A terbium-(2-pyrazinecarboxylate)-oxalate complex was formed as a minor phase from one of the batches. Indeed, the formation of ox^{2-} in the reaction medium occurred under hydrothermal conditions (Scheme 2), as explained below. In addition, using the same experimental conditions, but starting with europium(III) or terbium(III) nitrates and 2-Hpzc and oxalic acid (H_2ox), we have only obtained lanthanide-oxalate compounds (as revealed by FT-IR, not shown).

The formulation of compounds **1**−**7** as $[Ln_2(2,3\text{-pzdc})_2(ox)(H_2O)_2]_n$ and compound **8** as $[Tb_2(2\text{-pzc})_4(ox)(H_2O)_6]\cdot 10H_2O$ was performed on the basis of XRD studies together with elemental and thermogravimetric analysis, and FT-IR spectroscopy. Elemental analysis results and the FT-IR bands are given in the Experimental Section dedicated to the synthesis of the compounds. The FT-IR spectra are displayed in Supporting Information, Figure S1.

Under the used reaction conditions (150 °C, 1 day), 2,3-H_2pzdc was partially decomposed into 2-pzc^- and ox^{2-} (Scheme 2). This work gives clear evidence of the decarboxylation of 2,3-H_2pzdc, as shown by the isolation of compounds **1**−**8** that incorporate ox^{2-}, and in the case of compound **8** also by the presence of 2-pzc^-. This phenomenon was also found by Lee et al.[11,33] for 3,5-pyridinedicarboxylic and 2,4-pyridinedicarboxylic acids which, under hydrothermal conditions (180 °C, 3−6 days), gave rise to the formation of ox^{2-} that was coordinated in the lanthanide compounds obtained. 2-Hpzc was also reported to decompose into ox^{2-} under hydrothermal synthesis (165 °C, 6 days) producing a 2D LnOF, $[Ln_2(2\text{-pzc})_2(ox)_2(H_2O)_2]_n$ [Ln(III) = Pr or Er],[21] and a 3D LnOF, $\{[Nd_4(ox)_4(NO_3)_2(OH)_2(H_2O)_2]\cdot 5H_2O\}_n$.[34] Moreover, in hydrazinium salts of pyrazinedicarboxylic or pyridinedicarboxylic acid, one of the carboxylic groups is susceptible to decomposition (loss of CO_2) because of the intramolecular hydrogen bond between the nitrogen atom and the carboxylic group in the ortho position.[35] Several approaches have been used to explain the formation of ox^{2-};[33] that is beyond the scope of this work.

3.2. Crystal Structure Description of the $[Ln_2(2,3\text{-pzdc})_2(ox)(H_2O)_2]_n$ 2D LnOF series. The synthesized LnOF compounds belonging to the $[Ln_2(2,3\text{-pzdc})_2(ox)(H_2O)_2]_n$ series were isolated predominantly as microcrystalline powder materials (Supporting Information, Figure S2). **1** and **2** were also obtained in the form of single-crystals whose structures were elucidated by single-crystal X-ray diffraction, in combination with thermogravimetric and CHN elemental analyses, and FT-IR. Phase purity, homogeneity of the bulk samples, and the unequivocal structural phase identification of the remaining materials were confirmed from PXRD (Figure 1). Systematic searches in the literature and in the Cambridge Structural Database (CSD, Version 5.30 − November 2008)[36] reveal that these LnOF materials constitute the first examples incorporating simultaneously anionic residues of 2,3-$pzdc^{2-}$ and ox^{2-}. Despite ox^{2-} being one of the most utilized ligands in the preparation of multidimensional LnOFs (the latest version of the CSD contains a total of 238 entries), only a handful of examples incorporate anionic residues of 2,3-$pzdc^{2-}$ (only 8 entries in the CSD): $[Ln(2,3\text{-pzdc})(OH)(H_2O)]$ [Ln(III) = Er or Yb] (2D),[6] $[Ln_2(2,3\text{-pzdc})_3(H_2O)]\cdot 2H_2O$ [Ln(III) = La, Pr, Nd or Eu] (3D),[7] $[Ln_2Zn(2,3\text{-pzdc})_4(H_2O)_6]\cdot 2H_2O$ [Ln(III) = Gd, Nd or Sm] (3D),[15] and $[Eu(2,3\text{-pzdc})(NO_3)(phen)(H_2O)]\cdot 2H_2O$ (2D).[16]

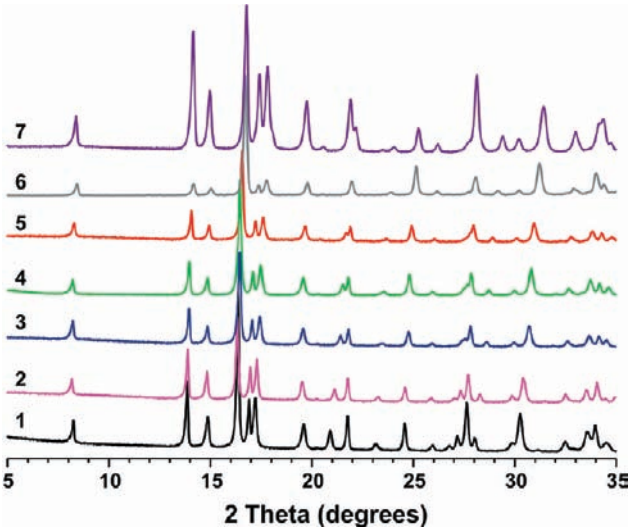

Figure 1. PXRD patterns for $[Ln_2(2,3\text{-pzdc})_2(ox)(H_2O)_2]_n$ [with Ln(III) = Ce (**1**), Nd (**2**), Sm (**3**), Eu (**4**), Gd (**5**), Tb (**6**), or Er (**7**)].

$[Ln_2(2,3\text{-pzdc})_2(ox)(H_2O)_2]_n$ LnOFs are isomorphous, crystallizing in the monoclinic $C2/m$ space group (Table 1). Even though crystal structures have been fully determined and refined for the Ce^{3+}- (**1**) and Nd^{3+}- (**2**) based materials, the crystallographic description will be focused on $[Ce_2(2,3\text{-pzdc})_2(ox)(H_2O)_2]_n$ (**1**), with the structural features emphasized for this compound being applicable for the remaining members of the series of materials.

$[Ce_2(2,3\text{-pzdc})_2(ox)(H_2O)_2]_n$ (**1**) contains one crystallographically independent lanthanide center [Ce(1)] coordinated to two O-atoms of an ox^{2-} ligand [O(1) and $O(2)^{i}$], four O [O(3), $O(3)^{ii}$, $O(4)^{iii}$, and $O(4)^{iv}$] and two N-atoms [N(1) and $N(1)^{ii}$] belonging to three symmetry-related 2,3-$pzdc^{2-}$ residues, plus one O-atom of a water molecule [O(1W)]. This leads to a nine-coordination sphere, $\{CeN_2O_7\}$ [Figure 2a; symmetry operations: (i) $-x+1, -y+1, -z+1$; (ii) $x, -y+1, z$; (iii) $x-1/2, -y+1/2, z$; (iv) $x-1/2, y+1/2, z$], which resembles a highly distorted tricapped trigonal geometry (Figure 2b) with the

(33) Min, D.; Lee, S. W. *Inorg. Chem. Commun.* **2002**, *5*, 978–983.
(34) Zhang, L. Z.; Gu, W.; Li, B.; Liu, X.; Liao, D. Z. *Inorg. Chem.* **2007**, *46*, 622–624.
(35) Premkumar, T.; Govindarajan, S.; Pan, W. P. *Proceedings of the Indian Academy of Sciences-Chemical Sciences* **2003**, *115*, 103–111.
(36) Allen, F. H. *Acta Crystallogr., Sect. B* **2002**, *58*, 380–388. Allen, F. H.; Motherwell, W. D. S. *Acta Crystallogr., Sect. B* **2002**, *58*, 407–422.

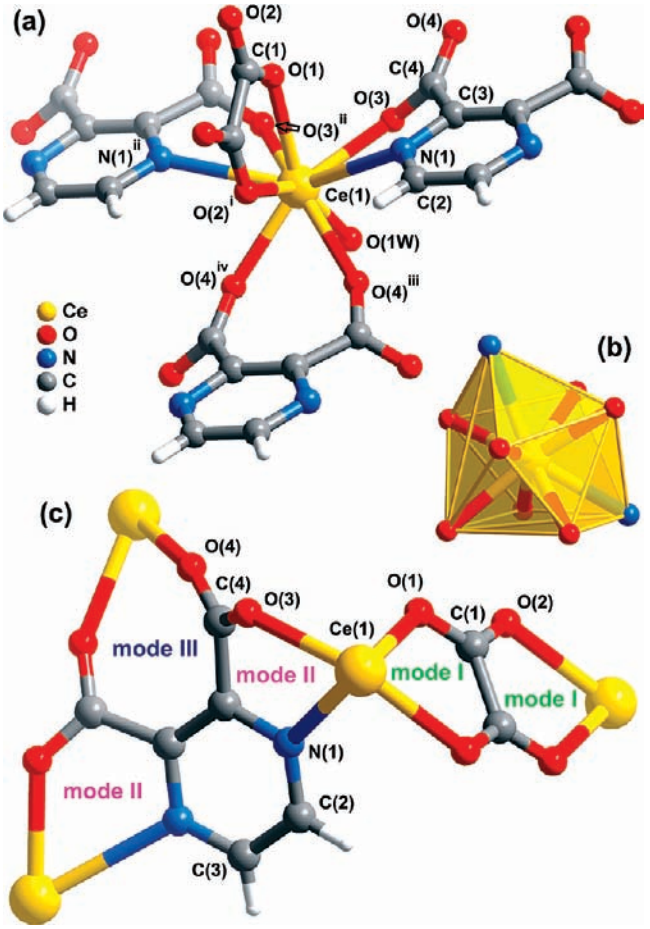

Figure 2. Schematic representation of the Ce^{3+} coordination environment and ligands' coordination modes found in $[Ce_2(2,3\text{-pzdc})_2(ox)(H_2O)_2]_n$ (**1**): (**a**) ball-and-stick representation showing the coordinated ligands, and the labeling scheme for all non-hydrogen atoms belonging to the asymmetric unit and to the first coordination sphere; (**b**) $\{CeN_2O_7\}$ polyhedral representation showing the distorted tricapped trigonal prism geometry; (**c**) ball-and-stick representation of the coordination modes of the two anionic ligands 2,3-$pzdc^{2-}$ and ox^{2-} showing the labeling scheme for the atoms belonging to the asymmetric unit. For selected bond lengths and angles see Supporting Information, Table S1. Symmetry operations used to generate equivalent atoms: (i) $-x+1, -y+1, -z+1$; (ii) $x, -y+1, z$; (iii) $x-1/2, -y+1/2, z$; (iv) $x-1/2, y+1/2, z$.

Ce−O bond lengths ranging from 2.41(3) to 2.581(5) Å, and the Ce−N bond distance being considerably longer, 2.872(2) Å (Supporting Information, Table S1). Additionally, the distortion of the lanthanide coordination sphere is clearly reflected by the internal (N,O)−Ce−(N, O) bond angles: while the O−Ce−O angles range between 66.06(16) and 153.45(15)°, the O−Ce−N angles can be found in the 58.48(12)-132.87(11)° range and the N−Ce−N angle is 139.62(11)° (Supporting Information, Table S1).

The ox^{2-} anionic ligand is structurally located at a symmetry plane and bridges two symmetry-related lanthanide cations via a *bis*-bidentate chelate interaction (**mode I**), behaving as a tetradentate ligand (Figure 2c). These *O,O*-chelate interactions are crystallographic equivalent with a bite angle of 66.06(16)° and originate an intermetallic $Ce(1)\cdots Ce(1)^{v}$ distance of 6.3706(10) Å [symmetry operation: (v) $-x+1, y, -z+1$]. The 2,3-$pzdc^{2-}$ anionic ligand connects three crystallographically equivalent Ce^{3+} centers via two distinct coordination modes, ultimately occurring in the crystal structure as a hexadentate ligand (Figure 2c): on the one hand, the heteroatoms of the aromatic ring form along, with the adjacent carboxylate groups, two equivalent *N,O*-chelate interactions (**mode II**) with the observed bite angles being of 58.48(12)°; on the other hand, two O-atoms of the two carboxylate groups, which are not involved in the previous coordination mode, coordinate via a bidentate interaction (**mode III**) with the O−Ce−O angle being of 68.81(12)°.

The intermetallic connectivity associated with the 2,3-$pzdc^{2-}$ organic ligand described above originates cationic monolayers, $\{_\infty^2[Ce(2,3\text{-pzdc})(H_2O)]^+\}$, having each Ce^{3+} center interconnected to other six neighboring symmetry-related cations, with the $Ce\cdots Ce$ distances being 6.7733(7) Å and 8.1744(11) Å (Figures 3a and 3b). The shorter distances between the lanthanide centers arise from the sequential combination of coordination **modes II** and **III**, while the longer is a direct consequence of the combination of two **modes II** (Figure 2c) leading to a brick-wall-like distribution of Ce^{3+} centers in the *ab* plane of the unit cell (Figure 3a). Two adjacent cationic monolayers $_\infty^2[Ce(2,3\text{-pzdc})(H_2O)]^+$ are interconnected via the ox^{2-} (coordination **mode I**) along the [001] direction of the unit cell (Figure 3c), imposing a $Ce\cdots Ce$ intermetallic distance of 6.3706(10) Å and leading to the formation of a neutral bilayer LnOF network, $_\infty^2[Ce_2(2,3\text{-pzdc})_2(ox)(H_2O)_2]$, placed in the *ab* plane of the unit cell (Figure 3d). It is of considerable importance to emphasize that this layered material can be envisaged as a true hybrid LnOF because there is a clear separation between the organic (2,3-$pzdc^{2-}$ ligand) and the inorganic components (two $\{CeN_2O_4\}$ polyhedra connected by one ox^{2-} anion) (Supporting Information, Figure S3).

A more systematic description of the neutral $_\infty^2[Ln_2(2,3\text{-pzdc})_2(ox)(H_2O)_2]$ bilayer can be attained by the use of a typical topological approach, that is, the crystal structure is converted into two connecting nodes (the lanthanide centers) and bridging rods (direct connections between nodes via the ox^{2-} and 2,3-$pzdc^{2-}$ anionic ligands).[37] This procedure, based in purely mathematical concepts applied to crystal chemistry, allows the immediate taxonomy of the isolated networks. Topological studies performed using the software package TOPOS[38] revealed that the bilayer (single penetrated 2-periodic net) is a 7-coordinated uninodal net with total Schäfli symbol $\{3^6.4^{12}.5^3\}$ (Figure 3e).

Individual $_\infty^2[Ce_2(2,3\text{-pzdc})_2(ox)(H_2O)_2]$ nets close pack along the [001] crystallographic direction with the coordinated water molecule O(1W) pointing to the interlayer space (Figure 4). It is important to note that the structural cohesion of this crystalline packing is further reinforced by the presence of highly directional $O-H\cdots O$ hydrogen bonds involving these water molecules from one layer and two symmetry-equivalent O(3) atoms of carboxylate groups belonging to the adjacent layer (bifurcated hydrogen bond interaction): $O(1W)\cdots O(3)^{iv}$ or $O(1W)\cdots O(3)^{v}$ with $d(O\cdots O) = 2.976(6)$ Å [symmetry codes: (iv) $-x+1, y, -z$; (v) $-x+1, 1-y, -z$].

(37) Wells, A. F. *Structural Inorganic Chemistry*, 4th ed.; Clarendon Oxford University Press: New York, 1975.
(38) Blatov, V. A.; Shevchenko, A. P. *TOPOS*, Version 4.0 Professional (beta evaluation); Samara State University: Samara, Russia, 2006.Blatov, V. A.; Shevchenko, A. P.; Serezhkin, V. N. *J. Appl. Crystallogr.* **2000**, *33*, 1193.

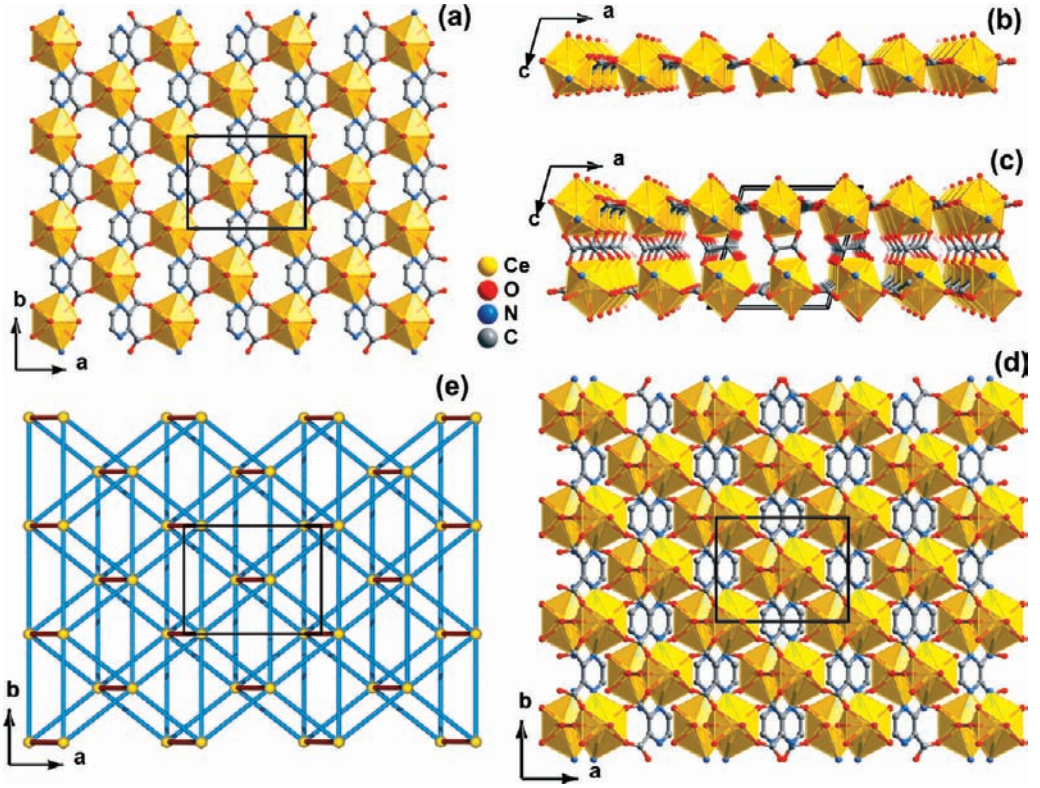

Figure 3. Mixed polyhedral (yellow) and ball-and-stick representation of the cationic monolayer $\{_{\infty}^{2}[Ce(2,3\text{-pzdc})(H_2O)]^{+}\}$ layer viewed along the (**a**) [001] and (**b**) [010] directions of the unit cell. Representation of the neutral $_{\infty}^{2}[Ce_2(2,3\text{-pzdc})_2(ox)(H_2O)_2]$ bilayer viewed along the (**c**) [010] and (**d**) [001] directions of the unit cell. (**e**) Topological representation of the $_{\infty}^{2}[Ce_2(2,3\text{-pzdc})_2(ox)(H_2O)_2]$ bilayer: the lanthanide centers were taken as the nodes (in yellow), and connections between nodes via anionic ligands 2,3-$pzdc^{2-}$ and ox^{2-} were replaced by blue and brown rods, respectively.

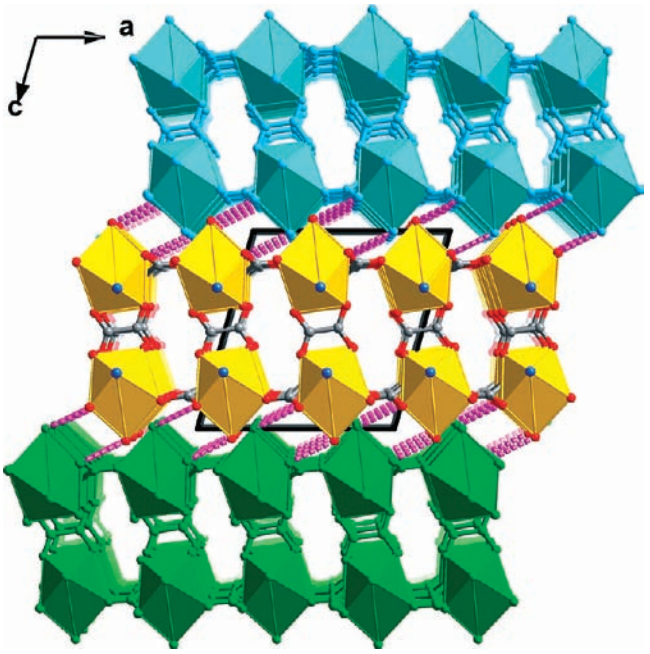

Figure 4. Crystal packing of $[Ce_2(2,3\text{-pzdc})_2(ox)(H_2O)_2]_n$ (**1**) viewed in perspective along the [010] crystallographic direction. Adjacent layers are represented in different colors and the interlayer hydrogen bonds as purple dashed lines. Hydrogen atoms belonging to the ligands have been omitted for clarity purposes.

3.3. Crystal Structure Description of the Discrete Complex $[Tb_2(2\text{-pzc})_4(ox)(H_2O)_6]\cdot 10H_2O$ (8).

The compound formulated as $[Tb_2(2\text{-pzc})_4(ox)(H_2O)_6]\cdot 10H_2O$ (**8**) represents, to the best of our knowledge, the first example of a binuclear discrete complex containing simultaneously 2-pzc^{-} and ox^{2-} (Figure 5). Meticulous searches in the literature and in the CSD[36] reveal that despite the large use of 2-pzc^{-} and ox^{2-} in the preparation of discrete complexes and multidimensional MOFs (the latest version of the CSD contains a total of 150 and 2195 entries for 2-pzc^{-} and ox^{2-}, respectively) there are only three compounds simultaneously containing 2-pzc^{-} and ox^{2-}: two are isostructural 2D LnOF materials, $_{\infty}^{2}[Ln_2(2\text{-pzc})_2(ox)_2(H_2O)_2]$ [Ln(III) = Pr or Er][21] while the other compound comprises a discrete anionic

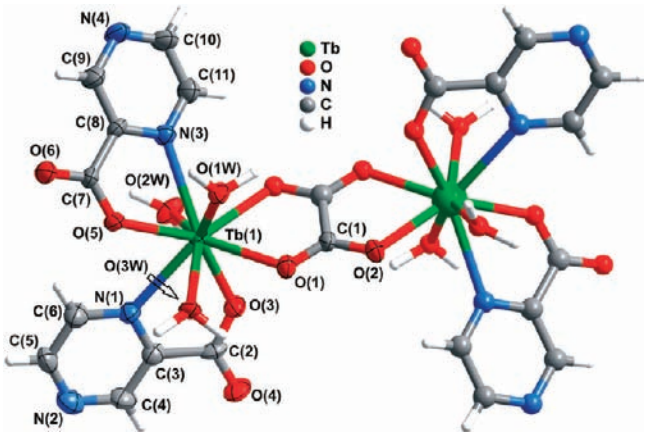

Figure 5. Mixed ellipsoid and ball-and-stick representation of the binuclear complex $[Tb_2(2\text{-pzc})_4(ox)(H_2O)_6]$ showing the labeling scheme for all non-hydrogen atoms belonging to the asymmetric unit. Thermal ellipsoids are draw at the 50% probability level. For selected bond lengths and angles see Supporting Information, Table S2.

vanadium complex, $[NH_3(CH_2)_2NH_3][VO(O_2)(2\text{-pzc})(ox)]\cdot 2H_2O$.[39]

The two symmetry-related lanthanides are coordinated at two *N,O*-chelating 2-pzc$^-$ ligands [N(1),O(3) and N(3), O(5) with bite angles of 63.19(18)° and 63.91(17)°, respectively], three water molecules [O(1W), O(2W), and O(3W)] and one *O,O*-chelating ox^{2-} ligand [O(1),O(2) with a bite angle of 66.84(17)°], leading to a nine coordination sphere, $\{TbN_2O_7\}$ (Figure 5 and Supporting Information, Table S2). The ox^{2-} anionic ligand is structurally located at an inversion center and bridges the two symmetry-related Tb^{3+} centers via a *bis*-bidentate chelate interaction being, thus, the responsible for the formation of the discrete binuclear complex. The Tb(1)···Tb(1)^{i} intermetallic distance is of 6.3000(5) Å [symmetry transformation: (i) $-x+1$, $-y+2$, $-z+2$]. The coordination environment of Tb^{3+}, $\{TbN_2O_7\}$, can be envisaged as a highly distorted tricapped trigonal prism as in compounds **1** to **7**, with the Tb−O bond distances ranging from 2.326(5) Å and 2.451(5) Å; the two Tb−N bonds are considerably longer, 2.677(6) Å and 2.681(6) Å for Tb(1)−N(1) and Tb(1)−N(3), respectively (Figure 5 and Supporting Information, Table S2). Similar to that observed in **1**, the distortion of the metallic coordination environment is undoubtedly reflected in the internal (N,O)−Tb−(N,O) bond angles: while the O−Tb−O angles range from 66.53(17)° to 141.3(2)°, the O−Tb−N angles are instead in the 63.91(17)°−142.30(18)°; the N(1)−Tb−N(3) angle is of 116.57(19)° (Supporting Information, Table S2).

The close packing of individual $[Tb_2(2\text{-pzc})_4(ox)(H_2O)_6]$ complexes is mediated by a number of intermolecular interactions, in particular strong and highly directional O−H···O and O−H···N hydrogen bonds involving the coordinated water molecules [O(1W), O(2W), and O(3W)] as donors and carboxylate oxygen atoms [O(6) and O(4)], and pyrazine groups as acceptors, respectively: O(1W)−H(1B)···O(6)^{iii}, O(2W)−H(2A)···O(4)^{iv}, and O(3W)−H(3B)···N(4)^{vii} [symmetry transformations: (iii) $-x+1$, $-y+2$, $-z+1$; (iv) $-x+1$, $-y+1$, $-z+2$; (vii) $x-1$, y, z; see Table 2 for more details]. These interactions lead to the formation of a porous 3D hydrogen bonding network with channels running along the [100] and [001] directions of the unit cell, which are filled by uncoordinated water molecules of crystallization [O(4W), O(5W), O(6W), O(7W), and O(8W)] (Figure 6a and Supporting Information, Figures S4 and S5). Water molecules of crystallization are further involved in a series of strong and highly directional O−H···O hydrogen-bonding interactions, thus ensuring overall structural cohesion of the crystal structure (Figure 6a and Supporting Information, Figure S6). Remarkably, the five crystallographically independent uncoordinated water molecules are engaged in cooperative water-to-water hydrogen-bonding interactions leading to the formation of pentameric water clusters, $(H_2O)_5$, as depicted in Figure 6b. Two adjacent pentameric clusters are further interacting with coordinated water molecules originating a cluster comprising 16 water molecules, $(H_2O)_{16}$, which can be more systematically represented by the graph set motif

Table 2. Hydrogen Bonding Geometry[a] for $[Tb_2(2\text{-pzc})_4(ox)(H_2O)_6]\cdot 10H_2O$ (**8**)[b]

D−H···A	*d*(H···A)	*d*(D···A)	∠(DHA)
O(1W)−H(1A)···O(7W)^{ii}	1.66(2)	2.643(8)	166(7) [c]
O(1W)−H(1B)···O(6)^{iii}	1.73(2)	2.710(7)	165(7)
O(2W)−H(2A)···O(4)^{iv}	1.80(2)	2.795(8)	172(9)
O(2W)−H(2B)···O(6W)^{v}	1.82(4)	2.768(9)	158(9) [c]
O(3W)−H(3A)···O(4W)^{vi}	1.81(2)	2.795(7)	170(8) [c]
O(3W)−H(3B)···N(4)^{vii}	1.82(3)	2.774(8)	159(6)
O(4W)−H(4A)···N(2)	1.86(3)	2.844(9)	167(10)
O(4W)−H(4B)···O(3W)^{viii}	2.08(5)	2.947(8)	144(7) [c]
O(4W)−H(4B)···O(1W)^{viii}	2.39(7)	3.094(8)	127(6) [c]
O(4W)−H(4B)···O(1)^{viii}	2.60(8)	3.372(8)	134(8) [c]
O(5W)−H(5A)···O(2)^{viii}	1.87(2)	2.861(8)	170(10)
O(5W)−H(5B)···O(4W)	1.92(4)	2.884(9)	162(10) [c]
O(6W)−H(6A)···O(5W)	1.89(4)	2.860(10)	162(11) [c]
O(6W)−H(6B)···O(4)	2.02(7)	2.934(10)	151(11)
O(7W)−H(7A)···O(8W)^{vi}	1.77(5)	2.735(14)	160(11) [c]
O(7W)−H(7B)···O(3)^{iv}	1.84(5)	2.799(9)	159(11)
O(7W)−H(7B)···O(4)^{iv}	2.55(8)	3.366(9)	138(9)
O(8W)−H(8A)···O(5W)^{ix}	1.79(4)	2.782(11)	170(21) [c]
O(8W)−H(8B)···O(6)^{vii}	1.82(8)	2.780(11)	159(18)

[a] Distances in angstrom and angles in degrees. [b] Symmetry transformations used to generate equivalent atoms: (ii) x, $y+1$, z; (iii) $-x+1$, $-y+2$, $-z+1$; (iv) $-x+1$, $-y+1$, $-z+2$; (v) $x+1$, y, z; (vi) $-x+1$, $-y+1$, $-z+1$; (vii) $x-1$, y, z; (viii) x, $y-1$, z; (ix) $-x$, $-y+1$, $-z+1$ [c] Hydrogen bonds only involving water molecules and which originate the water cluster.

$[C_5^5(11)]_2(S)_2R_4^4(8)$ (Supporting Information, Figure S7).[40] Despite recent reports that describe various types of discrete water clusters (such as tetramers, pentamers, hexamers, octamers, decamers, dodecamers) and a few polymeric clusters (essentially infinite chains), the description of large ordered aggregates of water molecules are much more scarce and, to the best of our knowledge, the $(H_2O)_{16}$ water cluster found in $[Tb_2(2\text{-pzc})_4(ox)(H_2O)_6]\cdot 10H_2O$ is unprecedented. Isolation of this compound was only attained at low temperature (ca. 4 °C), leading to the formation of the $(H_2O)_{16}$ water cluster and being indicative of a slow kinetic process.

3.4. Infrared Spectroscopy. The FT-IR spectra of compounds **1** to **7** are very similar as observed in Supporting Information, Figure S1 and by the main vibrational bands listed in the Experimental Section. FT-IR bands sensitive to metal coordination have been tentatively assigned based on those found in the literature for compounds with 2,3-H_2pzdc,[10] 2-Hpzc[19], and H_2ox.[41] The asymmetric stretching vibrational bands of carboxylate anions $\nu_{as}(CO_2^-)$ are assigned to the very strong bands in the 1681−1602 cm^{-1} range, while the symmetric stretching $\nu_s(CO_2^-)$ corresponds to the strong bands around 1370 and 1360 cm^{-1} and the medium band around 1310 cm^{-1}. For **8**, while the asymmetric mode $\nu_{as}(CO_2^-)$ is observed at 1619 cm^{-1}, the symmetric $\nu_s(CO_2^-)$ one appears at 1374 and 1315 cm^{-1}. The FT-IR bands centered at 1714 cm^{-1} (2,3-H_2pzdc), 1720 cm^{-1} (2-Hpzc) and 1684 cm^{-1} (H_2ox) in the spectra of the free ligands, assigned to stretching vibrations of the non ionized carboxylic group, are absent in the FT-IR spectra of **1**−**8**, confirming that the ligands are completely ionized, in agreement with the crystal structures. In the case of **8**, a very broad band is observed above 3000 cm^{-1} (maximum at 3365 cm^{-1}) and attributed to the characteristic ν(OH)

(39) Tatiersky, J.; Schwendt, P.; Sivak, M.; Marek, J. *Dalton Trans.* **2005**, 2305–2311.

(40) Bernstein, J.; Davis, R. E.; Shimoni, L.; Chang, N. L. *Angew. Chem., Int. Ed. Engl.* **1995**, *34*, 1555–1573.

(41) Shi, F. N.; Cunha-Silva, L.; Hardie, M. J.; Trindade, T.; Paz, F. A. A.; Rocha, J. *Inorg. Chem.* **2007**, *46*, 6502–6515.

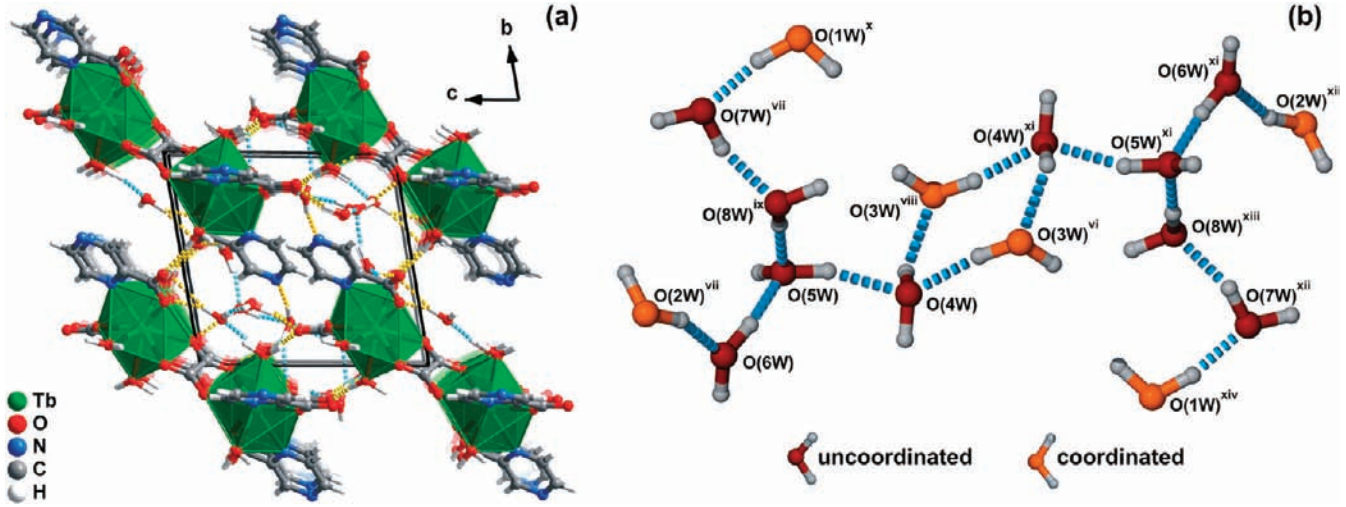

Figure 6. (**a**) Mixed polyhedral (green) and ball-and-stick representation of the crystal packing of $[Tb_2(2\text{-pzc})_4(ox)(H_2O)_6]\cdot 10H_2O$ (**8**) viewed in perspective along the [100] direction of the unit cell. Hydrogen bonds are represented as dashed lines (blue: interaction involving the uncoordinated water molecules; yellow: remaining hydrogen bonds). (**b**) The $(H_2O)_{16}$ cluster, with the oxygen atoms shown as red and orange for the uncoordinated and coordinated water molecules, respectively. Table 2 summarizes the hydrogen bonding geometry details. Symmetry transformations used to generate equivalent atoms: (vi) $-x+1, -y+1, -z+1$; (vii) $x-1, y, z$; (viii) $x, y-1, z$; (ix) $-x, -y+1, -z+1$; (x) $x-1, y-1, z$; (xi) $x-1, y-1, z-1$; (xii) $x-2, -y, -z+1$; (xiii) $x+1, y-1, z$; (xiv) $-x+2, -y+1, -z+1$.

stretching vibrational band related with the various water molecules. For **1** to **7**, a narrow band is visible above 3400 cm^{-1} (maximum peaking at 3483 cm^{-1}) associated with the highly defined environment of the hydrogen-bonded water molecules as shown by the crystal structures.

3.5. Thermal Properties. The thermal stability of **4** and **6** was examined by thermogravimetric analyses (TGA) in the 30−800 °C range. Thermograms show similar profiles and are provided as Supporting Information, Figure S8. The compounds are thermally stable up to 220 °C, with the first weight loss between 220 and 390 °C (4.9% for **4** and 4.7% for **6**), corresponding to the release of two coordinated water molecules (calcd 4.7% for **4** and **6**). The second weight loss, between 390 and 625 °C (50.8% for **4** and 49.4% for **6**), is attributed to the thermal decomposition of the organic components (calcd: 48.9% for **4** and 48.1% for **6**), leading to the formation of the stoichiometric amounts of Ln_2O_3 (total weight loss: 49.2% for **4** and 50.6% for **6**; calcd: 50.8% for **4** and 52.7% for **6**).

3.6. Diffuse Reflectance Spectroscopy. The diffuse reflectance spectra of compounds **1**−**7** and of free ligands are shown in the Supporting Information, Figure S9. For **1**, the large broad absorption band, in the range 300−500 nm, is ascribed to the allowed $4f^1 \rightarrow 5d^1$ transition. The spectra of **2** to **7** consist of a large broad absorption band in the UV region, approximately at 250−390 nm (peaks around 260, 310, and 360 nm), and of the Ln^{3+} characteristic intra-$4f^N$ transitions also detected for **2**−**4** and **7**. The spectrum of 2,3-H_2pzdc (very similar to that of 2-Hpzc, not shown) exhibits a similar band in the UV region, 250−365 nm peaking around 260 and 330 nm. The H_2ox ligand presents a narrower absorption band, ranging from 250 to 315 nm (peak around 260 nm). Therefore the observed band in the UV region of the prepared compounds and of the ligands can be assigned to electronic transitions from the ground-state level S_0 to the excited level S_1 of the ligands. Additionally, since the peak at 330 nm in 2,3-H_2pzdc shifts toward higher wavelengths in the prepared compounds (360 nm), it suggests an effective interaction between the lanthanide cations and this organic ligand.

3.7. Photoluminescence Studies. Photoluminescence measurements were performed in solid state for the Nd^{3+}, Sm^{3+}, Eu^{3+}, Gd^{3+}, and Tb^{3+} compounds. It was not possible to detect emission for the Ce^{3+} compound, neither at room temperature nor at 12 K.

The room temperature excitation spectra of compounds **2** and **3** are shown in Figure 7, monitored around the Ln^{3+} more intense emission lines, $^4F_{3/2} \rightarrow {}^4I_{11/2}$ (Nd^{3+}) and $^4G_{5/2} \rightarrow {}^6H_{9/2}$ (Sm^{3+}). They exhibit the typical transition lines from the $^4I_{9/2}$ and $^6H_{5/2}$ ground-states to various excited states of the Nd^{3+} and Sm^{3+} cations, respectively, along with a large broad band ranging from 250 to 400 nm (peaking at 320 and 370 nm for **2**, and 275, 310, and 360 nm for **3**) ascribed to the electronic transitions of the ligands, as discussed in detail below. The detection of this band together with its higher relative intensity points to a more efficient luminescence sensitization via the ligands excited states than the direct intra-$4f^N$ excitation (mainly for **3**).

Figure 8 illustrates the room temperature emission spectra of compounds **2** and **3**. The spectrum of compound **2** shows the characteristic emission lines of Nd^{3+} in the NIR region attributed to the $^4F_{3/2} \rightarrow {}^4I_{11/2,13/2}$ transitions, with the transition at 1064 nm ($^4F_{3/2} \rightarrow {}^4I_{11/2}$) being the strongest one. The emission spectrum of **3** is composed of a series of straight lines assigned to the Sm^{3+} $^4G_{5/2} \rightarrow {}^6H_{5/2,7/2,9/2,11/2}$ transitions. The emission features of both materials display an additional large broad band ranging from 380 to 540 nm, which arises from excited states of the ligands, as it may be inferred for **3** from the excitation spectrum monitored at 420 nm (Figure 7, gray line). A detailed discussion about that assignment is performed below. The NIR Nd^{3+} emission could be easily quenched by CH, OH, or NH oscillators, that act as nonradiative channels for the metal cation excited levels. Actually, few examples reporting NIR

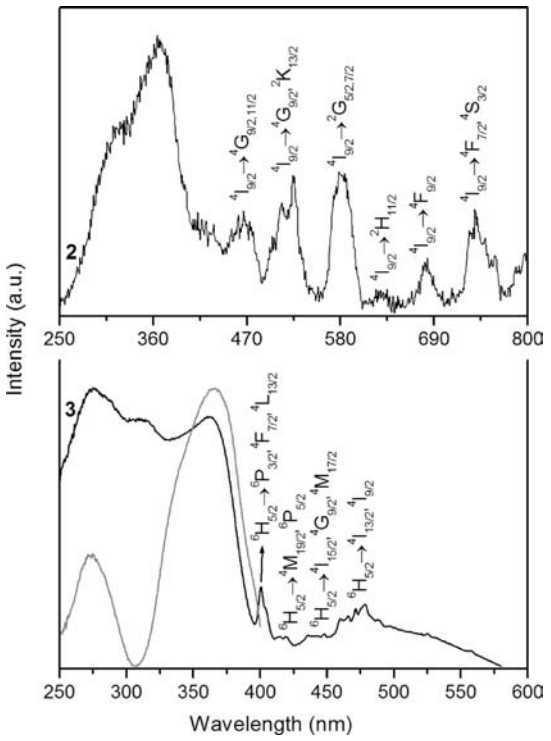

Figure 7. Room temperature excitation spectra of $[Nd_2(2,3\text{-pzdc})_2(ox)(H_2O)_2]_n$ (**2**) and $[Sm_2(2,3\text{-pzdc})_2(ox)(H_2O)_2]_n$ (**3**) monitored at 1064 and 643 nm, respectively. The gray line shows the excitation spectrum of **3** monitored at 420 nm.

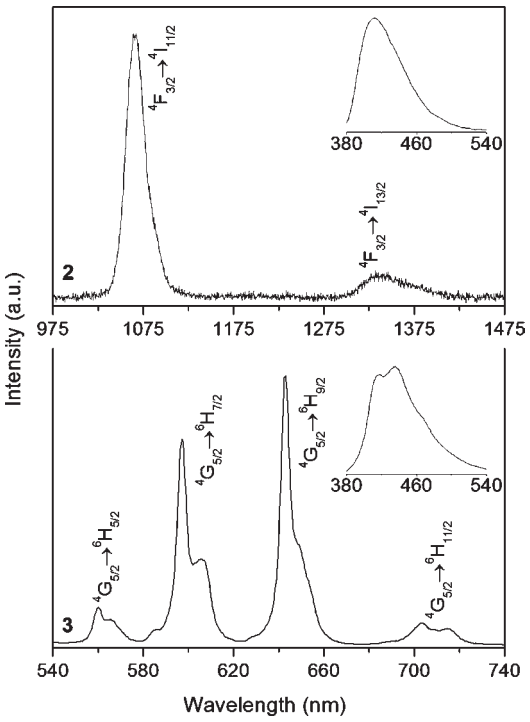

Figure 8. Room temperature emission spectra of $[Nd_2(2,3\text{-pzdc})_2(ox)(H_2O)_2]_n$ (**2**) and $[Sm_2(2,3\text{-pzdc})_2(ox)(H_2O)_2]_n$ (**3**) excited at 365 and 310 nm, respectively. The insets show the emission spectra in the region 380−540 nm, excited at the same wavelengths.

Nd^{3+} emission at room temperature in metal-organic frameworks can be found in the literature.[42]

To further characterize the origin of the band centered at 420 nm observed in the emission spectra of the Nd^{3+} and Sm^{3+} compounds, a detailed study was performed for the Gd^{3+} compound (**5**). This experimental procedure is based on the fact that the Gd^{3+} excited levels have energies much higher than those typical of ligand singlet and triplet states, disabling, therefore, any ligand−to−metal energy transfer process and allowing the ligand levels to be distinguished.

The emission spectra of **5** recorded at 12 K (Figure 9A) display two broad bands, peaking around 407 and 528 nm, ascribed to two triplet levels, in accord to the time delay (0.05 ms) of the corresponding time-resolved spectra shown in Figure 9B. The emission dependence with the excitation energy (Figure 9C), together with the diffuse reflectance data of the free ligands (Supporting Information, Figure S9), permit to assign unequivocally those two bands to the lowest-energy triplet levels of the 2,3-H_2pzdc and H_2ox ligands, leading to the construction of the energy diagram depicted in Figure 10. The emission decay curves of **5** detected at 12 K (Supporting Information, Figure S10), monitored around 520 and 450 nm and excited at 283 nm, reveal a non-exponential behavior, so that an average lifetime value (τ_{av}) was estimated considering the time value for which the maximum emission intensity is reduced to $1/e$. As a result, τ_{av} values of 2.006 ± 0.005 and 0.805 ± 0.005 ms were estimated for the 2,3-H_2pzdc and H_2ox triplet states, respectively. Such long-lived emissions are in good agreement with the triplet nature assignment above.[43] The non-exponential behavior is in accordance with the presence of complex ligand-to-ligand and ligand-to-metal energy transfer mechanisms.

The presence of such energy transfer involving the H_2ox and 2,3-H_2pzdc excited states is well supported by the excitation spectra of **5** presented in Figure 9C. For excitation energies lower than $\approx 26880\ cm^{-1}$ only the component at 407 nm ($24570\ cm^{-1}$) could be observed. These spectra, monitored within the 407 and 528 nm components, exhibit a band ranging from 240 to 400 nm (peaking at 283, 312, and 365−372 nm) with different relative intensities for the region at higher energies (240−330 nm). These spectra resemble that observed for **3** (Figure 7, gray line). The low-energy component at 18939 cm^{-1} is excited with similar intensity in all the wavelength range, whereas the high-energy one is preferentially excited for 365−372 nm. These results and the diffuse reflectance data of the free

(42) Marchal, C.; Filinchuk, Y.; Chen, X. Y.; Imbert, D.; Mazzanti, M. *Chem.—Eur. J.* **2009**, *15*, 5273–5288. Zhou, R. S.; Ye, L.; Ding, H.; Song, H. F.; Xu, X. Y.; Xu, J. Q. *J. Solid State Chem.* **2008**, *181*, 567–575. Turta, C.; Melnic, S.; Bettinelli, M.; Shova, S.; Benelli, C.; Speghini, A.; Caneschi, A.; Gdaniec, M.; Simonov, Y.; Prodius, D.; Mereacre, V. *Inorg. Chim. Acta* **2007**, *360*, 3047–3054. Zhu, P.; Gu, W.; Liu, M. L.; Song, H. B.; Liu, X.; Gao, Y. Q.; Duan, H. Y.; Yan, S. P.; Liao, D. Z. *CrystEngComm* **2009**, *11*, 351–358. Zucchi, G.; Maury, O.; Thurey, P.; Ephritikhine, M. *Inorg. Chem.* **2008**, *47*, 10398–10406. Gandara, F.; Garcia-Cortes, A.; Cascales, C.; Gomez-Lor, B.; Gutierrez-Puebla, E.; Iglesias, M.; Monge, A.; Snejko, N. *Inorg. Chem.* **2007**, *46*, 3475–3484. Cheng, J. W.; Zheng, S. T.; Yang, G. Y. *Dalton Trans.* **2007**, 4059–4066. Sun, L. N.; Yu, J. B.; Zheng, G. L.; Zhang, H. J.; Meng, Q. G.; Peng, C. Y.; Fu, L. S.; Liu, F. Y.; Yu, Y. N. *Eur. J. Inorg. Chem.* **2006**, 3962–3973. Yang, J.; Yuo, Q.; Li, G. D.; Cao, J. J.; Li, G. H.; Chen, J. S. *Inorg. Chem.* **2006**, *45*, 2857–2865. Ying, S. M.; Mao, J. G. *Cryst. Growth Des.* **2006**, *6*, 964–968. Zhou, R. S.; Cui, X. B.; Song, J. F.; Xu, X. Y.; Xu, J. Q.; Wang, T. G. *J. Solid State Chem.* **2008**, *181*, 2099–2107.

(43) Bruno, S. M.; Ferreira, R. A. S.; Paz, F. A. A.; Carlos, L. D.; Pillinger, M.; Ribeiro-Claro, P.; Goncalves, I. S. *Inorg. Chem.* **2009**, *48*, 4882–4895. Lima, P. P.; Paz, F. A. A.; Ferreira, R. A. S.; Bermudez, V. D.; Carlos, L. D. *Chem. Mater.* **2009**, *21*, 5099–5111.

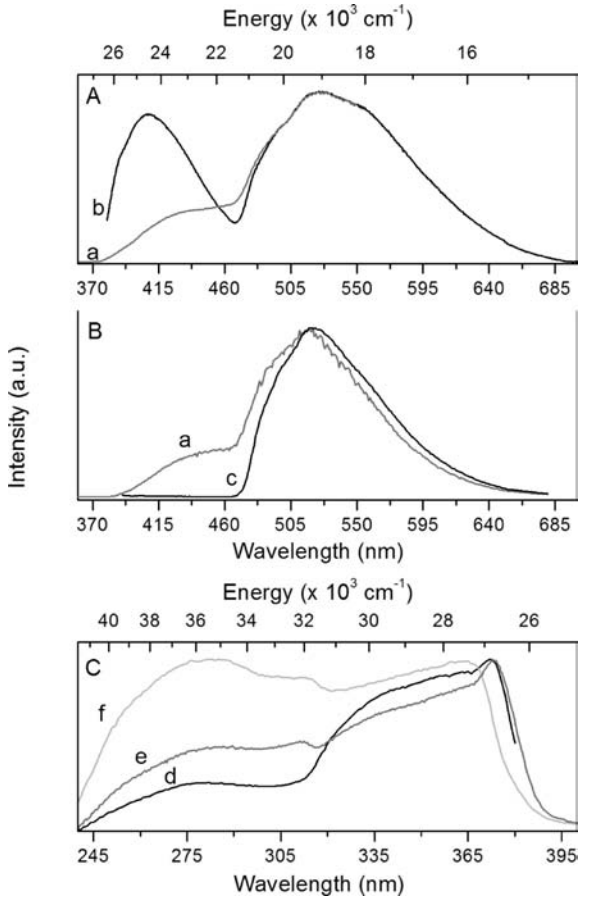

Figure 9. 12 K (A) Steady-state emission, (B) time-resolved emission (sample delay of 0.05 ms) and (C) excitation spectra of $[Gd_2(2,3\text{-pzdc})_2(ox)(H_2O)_2]_n$ (**5**), excited at (a) 283, (b) 365, and (c) 372 nm, and monitored at (d) 407, (e) 435, and (f) 528 nm, respectively.

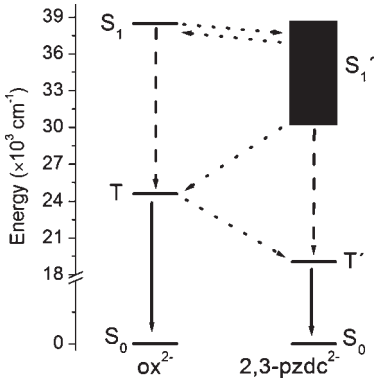

Figure 10. Schematic illustration of the energy diagram of H_2ox and 2,3-H_2pzdc in the compounds $[Ln_2(2,3\text{-pzdc})_2(ox)(H_2O)_2]_n$, showing the radiative (solid arrow) and nonradiative (dashed arrow) deactivation and the energy transfer between the two ligands (dotted arrow).

ligands (Supporting Information, Figure S9) point out that the lowest-energy triplet at 528 nm should be ascribed to the 2,3-H_2pzdc ligand (2,3-H_2pzdc absorbs in a much broader wavelength region compared to H_2ox). Moreover, complex energy transfer pathways occur between the singlet levels of the two ligands and between the triplet of 2,3-H_2pzdc and the one of H_2ox (Figure 10). The energy levels of the lowest-singlet excited states of the two ligands were obtained from the absorption edge [$0(S_0) \rightarrow 0(S_1)$] transitions on the

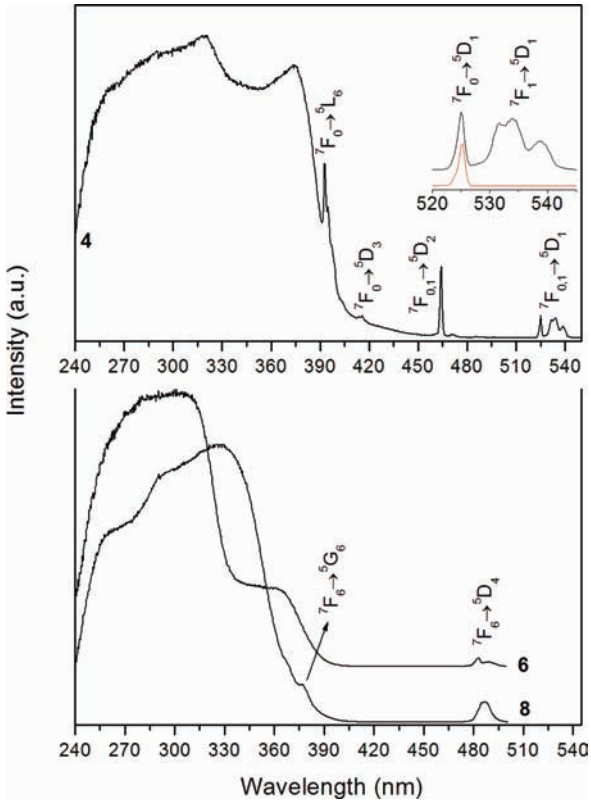

Figure 11. Room temperature excitation spectra monitored around 614 nm for $[Eu_2(2,3\text{-pzdc})_2(ox)(H_2O)_2]_n$ (**4**), and 544 nm for $[Tb_2(2,3\text{-pzdc})_2(ox)(H_2O)_2]_n$ (**6**) and $[Tb_2(2\text{-pzc})_4(ox)(H_2O)_6]\cdot 10H_2O$ (**8**). The inset shows a detailed view of the excitation spectrum of **4** in the range 520−545 nm at 300 K (black line) and 12 K (red line).

corresponding diffuse reflectance spectra (38462 cm^{-1} for H_2ox and 38462−30303 cm^{-1} for 2,3-H_2pzdc). The energy values of the singlet and triplet levels found for 2,3-H_2pzdc are in good agreement with those reported for the similar 2-Hpzc molecule in $Ln(2\text{-pzc})_3\cdot nH_2O$ [Ln(III) = Eu or Gd], 37453 and 18444 cm^{-1} (experimental) or 37456 cm^{-1} and 18967 cm^{-1} (theoretical), respectively.[17] The energy of the triplet states is higher than the emitting excited states of Nd^{3+} ($^4F_{3/2} \approx 11400$ cm^{-1}) and Sm^{3+} ($^4G_{5/2} \approx 17850$ cm^{-1}) confirming the suitability of the ligands as sensitizers for these lanthanides. Comparing the energy gap between the triplet states of the ligands and the Nd^{3+} and Sm^{3+} emissive states, 2,3-H_2pzdc is a better sensitizer than H_2ox. Furthermore, the energy gap between the 2,3-H_2pzdc triplet level and Sm^{3+} emissive state is considerably lower than that involving H_2ox triplet level and Nd^{3+} emissive state, which may explain the low intensity in the excitation spectrum of **2** for the region 250−275 nm and a better sensitization of Sm^{3+}.

Figure 11 shows the room temperature excitation spectra of **4**, **6**, and **8** monitored around the more intense emission line, 614 nm for Eu^{3+} and 544 nm for Tb^{3+}. The excitation spectra show a large broad band in the region 240−400 nm ascribed to the electronic transitions of the ligands, with the $^7F_{0,1} \rightarrow {}^5L_6, {}^5D_{3-0}$, or $^7F_6 \rightarrow {}^5G_6, {}^5D_4$ transitions being also detected. Again, the detection of this band together with its higher intensity relatively to the intra-4f^N transitions, points out a more efficient luminescence sensitization via the ligands excited states than the direct intra-4f^N excitation.

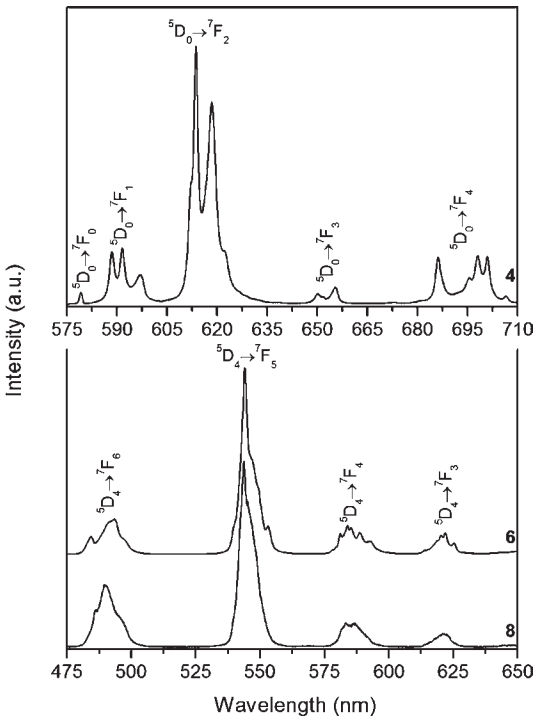

Figure 12. Room temperature emission spectra excited at 319 nm for $[Eu_2(2,3\text{-pzdc})_2(ox)(H_2O)_2]_n$ (**4**), 280 nm for $[Tb_2(2,3\text{-pzdc})_2(ox)(H_2O)_2]_n$ (**6**), and 330 nm for $[Tb_2(2\text{-pzc})_4(ox)(H_2O)_6]\cdot 10H_2O$ (**8**).

The room temperature emission spectra of **4**, **6**, and **8** (Figure 12), excited at 319 nm (for **4**), 280 nm (for **6**), and 330 nm (for **8**), exhibit a series of straight lines assigned to intra-$4f^6$ (Eu^{3+}) and intra-$4f^8$ (Tb^{3+}) transitions. Changing the excitation wavelength along the broadband or the intra-$4f^N$ does not produce significant changes in the emission spectra, indicating that all the Ln^{3+} cations lie in the same average local environment, as previously described in the crystallographic part. Although, the large value found for the full width at half-maximum (fwhm) of the non-degenerated $^5D_0 \rightarrow {}^7F_0$ transition in **4**, either at room temperature or at 12 K ($25.0 \pm 0.3\ cm^{-1}$), points to a continuous distribution of closely similar local environment for the Eu^{3+} ions. The energy of the triplet states ($24570\ cm^{-1}$ for H_2ox and $19048\ cm^{-1}$ for 2,3-H_2pzdc) is higher than the Eu^{3+} emitting excited state ($^5D_0 \approx 17300\ cm^{-1}$), but the triplet level of 2,3-H_2pzdc lies below the Tb^{3+} emitting excited state ($^5D_4 \approx 20500\ cm^{-1}$), disabling efficient (2,3-H_2pzdc)-to-Tb^{3+} energy transfer. This fact supports the lower intensity for the region 315−390 nm in the excitation spectrum of **6** when compared with **2**−**4**. Emission from the ligands could not be detected for the Eu^{3+} and Tb^{3+} compounds at room temperature and at 12 K (not shown). This fact suggests that the ligand-to-lanthanide energy transfer process for compounds **4** and **6** is more efficient than that involving the Nd^{3+} and Sm^{3+} cations in **2** and **3**, or that a nonradiative deactivation of the excited levels of the ligands occurs in **4** and **6**.

The $^5D_0$ (Eu^{3+}) and $^5D_4$ (Tb^{3+}) decay curves were monitored within the more intense line of the $^5D_0 \rightarrow {}^7F_2$ and $^5D_4 \rightarrow {}^7F_5$ transitions, respectively, with excitations in the intra-$4f^N$ levels (464 nm for **4**; and 490 nm for **6**) and in the levels of the ligands (330 nm for **8**). The room temperature emission decay curves of **4** and **8** (Supporting Information, Figure S11) are well fitted by a single-exponential function. The emission decay curve of **6** does not reveal a single-exponential behavior for times below 0.15 ms, suggesting that the Tb^{3+} cations are accommodated in a continuous distribution of closely similar local sites, as referred above for compound **4**. We determined lifetime values of 0.333 ± 0.006 ms (for **4**), 0.577 ± 0.017 ms (for **6**), and 0.845 ± 0.007 ms (for **8**); these values are similar to those found for other LnOFs.[4,5]

The $^5D_0$ radiative (k_r) and nonradiative (k_{nr}) transition probabilities and the $^5D_0$ quantum efficiency (η) [$\eta = k_r/(k_r + k_{nr})$] can be estimated based on the emission spectrum and $^5D_0$ lifetime ($\tau_{exp}^{-1} = k_r + k_{nr}$).[13,44] The radiative contribution of the Eu^{3+}-based materials may be calculated from the relative intensities of the $^5D_0 \rightarrow {}^7F_{0-4}$ transitions (the $^5D_0 \rightarrow {}^7F_{5,6}$ branching ratios are neglected because of their poor relative intensity with respect to that of the remaining $^5D_0 \rightarrow {}^7F_{0-4}$ lines). The $^5D_0 \rightarrow {}^7F_1$ transition does not depend on the local ligand field and, therefore, may be used as a reference for the whole spectrum. An effective refractive index of 1.5 was used leading to $A_{01} \approx 50\ s^{-1}$; A_{01} stands for the Einstein's coefficient of spontaneous emission between the $^5D_0$ and the $^7F_1$ Stark levels. We found an η value of 0.14 for the Eu^{3+} emission in **4** ($k_r = 0.417\ ms^{-1}$, $k_{nr} = 2.59\ ms^{-1}$), exciting within the $^7F_0 \rightarrow {}^5D_2$ transition (464 nm) at room temperature.

The absolute emission quantum yields, ϕ, were measured for **3**, **4**, and **6** at room temperature under the excitation wavelengths that maximizes the emission of the lanthanide cation (315, 319, and 305 nm, respectively). The absolute emission quantum yield of **3** is lower than the detection limits of our equipment (< 0.01). The corresponding values found for the Eu^{3+} and the Tb^{3+} compounds are 0.13 ± 0.01 and 0.05 ± 0.01, respectively, similar values were found for other LnOFs.[4,5] Considering that, for the Eu^{3+} compound, all the emission arises from the $^5D_0$ level, the overall absolute emission quantum yield ($\phi_{overall}$) is the product of the sensitization efficiency of the ligand ($\phi_{transfer}$) and the $^5D_0$ quantum efficiency (η) ($\phi_{overall} = \phi_{transfer}\cdot\eta$).[45] As a result the $\phi_{transfer}$, which reflects the ligand-to-metal energy transfer efficiency, has a value of 0.93 ± 0.01.

4. Conclusions

A new series of 2D LnOFs, $[Ln_2(2,3\text{-pzdc})_2(ox)(H_2O)_2]_n$ [Ln(III) = Ce, Nd, Sm, Eu, Gd, Tb, or Er], has been prepared using hydrothermal synthesis. These materials represent the first example of bilayer networks containing 2,3-H_2pzdc in coordination polymers. Under the hydrothermal conditions used (150 °C, 1 day), 2,3-H_2pzdc was partially decomposed into ox^{2-} (which was included in **1**−**7**) and 2-pzc^-. This decarboxylation of 2,3-H_2pzdc is unequivocally proved by the isolation of the new discrete complex $[Tb_2(2\text{-pzc})_4(ox)(H_2O)_6]\cdot 10H_2O$ (**8**), obtained as a secondary material, which incorporates ox^{2-} and 2-pzc^-, as shown by the XRD studies. The latter compound co-crystallized with an unprecedented $(H_2O)_{16}$ water cluster. Upon UV excitation at room temperature

(44) Carlos, L. D.; Messaddeq, Y.; Brito, H. F.; Ferreira, R. A. S.; Bermudez, V. D.; Ribeiro, S. J. L. *Adv. Mater.* **2000**, *12*, 594–598. Carlos, L. D.; Ferreira, R. A. S.; Bermudez, V. D.; Ribeiro, S. J. L. *Adv. Mater.* **2009**, *21*, 509–534.

(45) Xiao, M.; Selvin, P. R. *J. Am. Chem. Soc.* **2001**, *123*, 7067–7073. Ambili Raj, D. B.; Biju, S.; Reddy, M. L. P. *J. Mater. Chem.* **2009**, *19*, 7976–7983.

the ligands sensitize the luminescence of the Nd^{3+}, Sm^{3+}, Eu^{3+}, and Tb^{3+} cations. The energy levels of the triplet states of 2,3-H_2pzdc and H_2ox, determined from the 12 K emission spectrum of the Gd^{3+} compound (**5**), are higher than the emitting excited states of Nd^{3+}, Sm^{3+}, and Eu^{3+}, being suitable as sensitizers for those lanthanides. In the case of the Tb^{3+} compound (**6**) the triplet level of 2,3-H_2pzdc lies below its emitting excited state leading to a sensitization pathway mainly through the H_2ox triplet state. Lifetime values of 0.333 ± 0.006 ms ($^5D_0$, for **4**), 0.577 ± 0.017 ms ($^5D_4$, for **6**), and 0.845 ± 0.007 ms ($^5D_4$, for **8**) and absolute emission quantum yields of 0.13 ± 0.01 (for **4**) and 0.05 ± 0.01 (for **6**) were obtained. A high efficiency of the ligands-to-Eu^{3+} energy transfer was estimated for **4** (0.93 ± 0.01).

Acknowledgment. We are grateful to *Fundação para a Ciência e a Tecnologia* (FCT, Portugal) for funding the R&D projects PTDC/QUI/65805/2006 and PTDC/QUI-QUI/098098/2008, for the financial support toward the purchase of the single-crystal diffractometer, and for the postdoctoral scholarship No. SFRH/BPD/14954/2004 (to P.S.-S.).

Supporting Information Available: X-ray crystallographic information (CIF format files) for compounds **1**, **2**, and **8**. Additional structural tables and figures. FT-IR and diffuse reflectance spectra. SEM images of **1**, **4**, and **6**. TGA curves of **4** and **6**. Emission decay curves of **4**−**6** and **8**. This material is available free of charge via the Internet at http://pubs.acs.org.